Joint Velocity-Growth Flow Matching for Single-Cell Dynamics Modeling

Dongyi Wang[1,*]**, Yuanwei Jiang**[1,*]**, Zhenyi Zhang**[2,*]**, Xiang Gu**[1,†]**, Peijie Zhou**[3,†]**, Jian Sun**[1,†]

[1]School of Mathematics and Statistics, Xi'an Jiaotong University, Xi'an, China
[2]LMAM and School of Mathematical Sciences, Peking University, Beijing, China.
[3]Center for Machine Learning Research, Peking University, Beijing, China.
{dongyiwang,jyw1578857771}@stu.xjtu.edu.cn; {xianggu,jiansun}@xjtu.edu.cn;
zhenyizhang@stu.pku.edu.cn; pjzhou@pku.edu.cn

Abstract

Learning the underlying dynamics of single cells from snapshot data has gained increasing attention in scientific and machine learning research. The destructive measurement technique and cell proliferation/death result in unpaired and unbalanced data between snapshots, making the learning of the underlying dynamics challenging. In this paper, we propose joint Velocity-Growth Flow Matching (VGFM), a novel paradigm that jointly learns state transition and mass growth of single-cell populations via flow matching. VGFM builds an ideal single-cell dynamics containing velocity of state and growth of mass, driven by a presented two-period dynamic understanding of the static semi-relaxed optimal transport, a mathematical tool that seeks the coupling between unpaired and unbalanced data. To enable practical usage, we approximate the ideal dynamics using neural networks, forming our joint velocity and growth matching framework. A distribution fitting loss is also employed in VGFM to further improve the fitting performance for snapshot data. Extensive experimental results on both synthetic and real datasets demonstrate that VGFM can capture the underlying biological dynamics accounting for mass and state variations over time, outperforming existing approaches for single-cell dynamics modeling.

1 Introduction

Inferring the latent dynamics of complex systems from sparse and noisy data is a fundamental challenge in science and engineering. In many domains, *e.g*., stock markets [1], climate systems [2], and biological processes [3–10], continuous trajectories are rarely fully observed by sensors. Instead, cross-sectional snapshot data collected at discrete time points are commonly provided. This challenge is especially important in single-cell RNA sequencing [11–15], where destructive sampling yields unpaired population-level snapshots across time without having the tracked individual cell fates. Furthermore, due to the mass changes during cellular development or response processes, observed data often exhibits mass unbalancedness across time, violating mass conservation. Consequently, reconstructing the time-evolving, unnormalized density function from limited samples has become an important research problem and attracted increasing attention [13, 14, 16].

Deep learning-based models for dynamics inference have demonstrated great potential [3, 7, 17–28]. These models typically employ ordinary or stochastic differential equations (ODEs or SDEs) parameterized by neural networks to approximate the velocity field governing density evolution. One class of methods, based on simulation [3, 17–19, 22, 23, 25, 29, 30], generates synthetic

---

*These authors contributed equally. †Corresponding authors.

trajectories by feeding initial data through neural networks and solving ODEs or SDEs numerically, and compares simulated results with observations for loss computation. However, these simulation-based methods rely heavily on numerical solvers during training, which significantly increases computational cost. In high-dimensional settings, the enlarged search space further exacerbates instability, hindering scalability and convergence. Another line of research focuses on simulation-free approaches [21, 28, 31–41], where the velocity field is trained efficiently by constructing conditional probability paths without trajectory simulation, yielding better efficiency and stability in training compared with simulation approaches.

Nevertheless, the simulation-free approaches mentioned above rely solely on the velocity field v, ignoring the unbalancedness of observed data, which can result in incorrect reconstruction of underlying dynamics or unsatisfying generation performance [25, 35, 40]. Distributional imbalance is a common phenomenon in single-cell dynamics, where cellular proliferation and death occur, thus necessitating the introduction of a growth term g to allow for mass increasing or decreasing. To address this, [42, 43] proposed to jointly learn velocity v and growth g by minimizing the Wasserstein-Fisher-Rao (WFR) metric [44, 45]. However, it mathematically enforces $v = \nabla g$, which lacks clear mechanistic justification in biological systems. Other WFR-inspired approaches [22, 25] design separate neural networks for v and g and prioritize fitting the distributions. However, these methods require heavy simulation during training, limiting their scalability to high dimensions.

In this paper, we propose joint Velocity-Growth Flow Matching (VGFM), a novel approach for single-cell dynamics modeling. VGFM aims to learn the joint state transition[2] and mass growth[3] of single-cell evolution by flow matching, as illustrated in Fig. 1. VGFM is based on the static semi-relaxed optimal transport that allows mass variation in building coupling between snapshots, for which we present a dynamic understanding that enables mass growth and state transition accomplished in two time periods, respectively. Based on this dynamic understanding, we build a joint transition and growth dynamics, in-heriting the optimal properties of semi-relaxed optimal transport. We then approximate the velocity
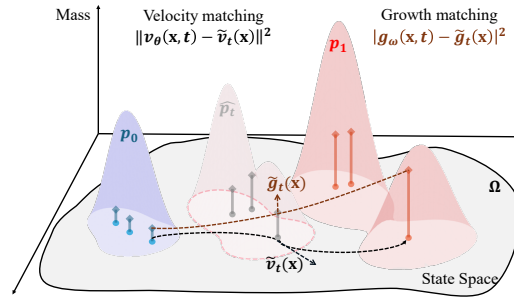

Figure 1: The goal of this paper is to learn a joint state transition (controlled by $v_\theta(\mathbf{x}, t)$) and mass growth (controlled by $g_\omega(\mathbf{x}, t)$) dynamics for single-cell evolution.

and growth in the built dynamics using neural networks with finite samples, yielding a joint velocity and growth flow matching framework. To further improve fitting performance for the single-cell snapshots, we employ a distribution fitting loss based on the Wasserstein distance. Thanks to the joint velocity and growth flow matching, our approach enjoys more stable training and better scalability to high dimensions, compared with simulation-based approaches. Extensive experiments on both synthetic and real single-cell datasets are conducted to evaluate our proposed approach. Experimental results demonstrate accurate dynamics reconstruction and superior performance achieved by VGFM over recent baselines.

2   Background and Related Works

This section revisits optimal transport, and reviews the flow-matching-based methods for single-cell and unbalancedness-aware distribution learning methods, which are mostly related to this paper.

Optimal transport. Given two distributions p_0 and p_1 on domain Ω satisfying $\int_\Omega p_0(\mathbf{x}) \, \mathrm{d}x = \int_\Omega p_1(\mathbf{x}) \, \mathrm{d}x$, the optimal transport [46] aims to find a joint distribution of p_0 and p_1, named coupling, such that the transport cost is minimized, formulated as the following optimization problem:

$$\min_{\pi \in U(p_0, p_1)} \int_{\Omega^2} c(\mathbf{x}_0, \mathbf{x}_1) \, \mathrm{d}\pi(\mathbf{x}_0, \mathbf{x}_1), \text{ s.t. } U(p_0, p_1) = \left\{ \pi \geq 0 : \mathrm{P}^0_\# \pi = p_0, \, \mathrm{P}^1_\# \pi = p_1 \right\}, \quad (1)$$

---

[2]State transition describes changes in gene expression in a cell.

[3]Mass growth means mass increasing or decreasing.

where c is the cost function. For a map T, we define $T_{\#}p_0(\mathbf{x}) = \int_{\mathbf{x}':T(\mathbf{x}')=\mathbf{x}} p_0(\mathbf{x}') \, d\mathbf{x}'$. Let $\mathbf{P}^i(\mathbf{x}_0, \mathbf{x}_1) = \mathbf{x}_i$ for $i = 0, 1$, then we have $\mathbf{P}^i_{\#}\pi(\mathbf{x}_i) = \int_{\Omega} \pi(\mathbf{x}_0, \mathbf{x}_1) \, d\mathbf{x}_i$ for $i = 0, 1$. When $c(\mathbf{x}_0, \mathbf{x}_1) = \|\mathbf{x}_0 - \mathbf{x}_1\|^2$, by Brenier's theorem [47], the optimal coupling can be expressed as $\pi^* = (\text{Id}, T^*)_{\#}p_0$, where T^* is called the Monge map.

Flow matching for learning single cell dynamics. Flow matching [31–33] is a simulation-free approach where the velocity field is trained efficiently by constructing conditional probability paths without trajectory simulation. Building on this foundation, further improvements have been achieved by incorporating optimal transport guidance [21, 34], considering unbalancedness [35], accounting for manifold structures [36], and approximating Schrödinger bridge via flow and score matching [39], all of which has been applied to model single-cell dynamics [21, 35, 36, 39]. Different from these methods, our method explicitly models the simultaneous matching of both the velocity field and the growth function, driven from our developed ideal joint state transition and mass growth dynamics, which does not require the construction of conditional probability paths like the above approaches.

Unbalancedness-aware distribution learning methods. Data imbalance is prevalent across a variety of domains, such as image synthesis and protein generation, motivating the development of flow matching models that account for unbalanced distributions [35, 40, 48]. However, these methods often do not model growth functions, which are essential in single-cell contexts. In the single-cell domain, several approaches have been proposed to model growth dynamics [5, 22, 42, 43, 49], yet they either fail to leverage the informative variations in cell abundance observable from snapshot data [42, 43], or rely heavily on computationally expensive simulations [5, 22, 49], limiting their scalability and efficiency. Differently, our method explicitly learns the growth function from observed snapshot data, yielding better performance for single cells than these methods as shown in experiments.

3 Method

Given the snapshot population of single cells, this paper aims to build the dynamic trajectory of single cells. Considering the unbalancedness between snapshot populations due to the undergo cell proliferation or death, we aim to build a model that can transform between unbalanced distributions by jointly learning a velocity field for controlling state transition and a growth function for controlling mass variation. Towards this goal, we propose joint Velocity-Growth Flow Matching (VGFM) based on semi-relaxed optimal transport to learn the dynamics of single cells. As illustrated in Fig. 2, we first present a decoupled understanding of state transition and mass growth for unbalanced dynamics based on semi-relaxed optimal transport (Figs. 2 (b), (d)), upon which we build a dynamic process between unbalanced distributions (Fig. 2 (c)). Finally, we propose the velocity and growth flow matching using the built dynamic process to learn the velocity and growth with samples (Fig. 2 (a)). Next, we first describe the unbalanced dynamics of single-cell data, and then discuss the details of each component of our method.

3.1 Unbalanced Dynamics of Single Cell

Given two adjacent snapshots of populations/distributions denoted as p_0 and p_1, if the system is balanced, the dynamics $\bar{p}_t(t \in [0, 1])$ between p_0 and p_1 can be generated by ODE $\frac{d\mathbf{x}_t}{dt} = v_t(\mathbf{x}_t)$ such that $\mathbf{x}_0 \sim p_0$ and $\mathbf{x}_1 \sim p_1$. Corresponding to this ODE, $\bar{p}_t$ is governed by continuity equation $\partial_t \bar{p}_t = -\nabla \cdot (\bar{p}_t v_t)$. However, in biological systems, cells can proliferate and die. Such behaviors can be captured by a time-dependent weight $w_t(\mathbf{x}_t)$ associated with the state transition, whose evolution is controlled by a growth function g, simulating cell proliferation or death processes:

$$\begin{cases} \frac{d\mathbf{x}_t}{dt} = v_t(\mathbf{x}_t), \\ \frac{d\log w_t(\mathbf{x}_t)}{dt} = g_t(\mathbf{x}_t). \end{cases} \tag{2}$$

Under this formulation, the unbalanced distribution dynamics p_t is generated jointly by the position $\mathbf{x}_t$ and the weight $w_t(\mathbf{x}_t)$. Specifically, $w_t(\mathbf{x}_t)$ models the variation of p_t against $\bar{p}_t$, i.e., $w_t(\mathbf{x}_t) = p_t(\mathbf{x}_t)/\bar{p}_t(\mathbf{x}_t)$ for $\bar{p}_t(\mathbf{x}_t) \neq 0$. Corresponding to Eq. (2), p_t is governed by

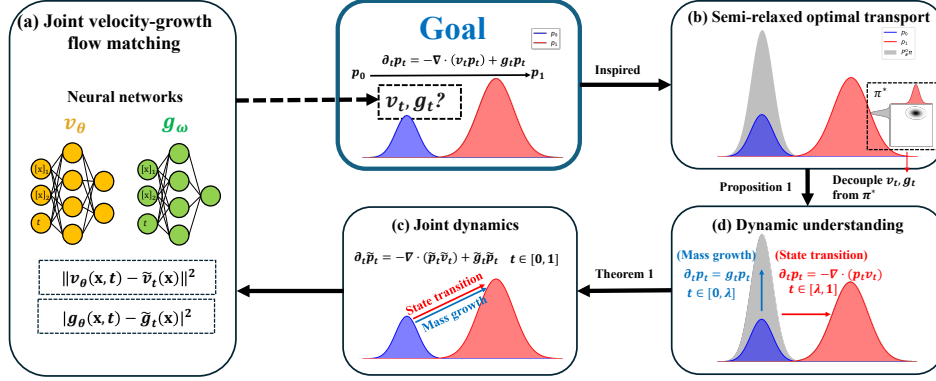$$\partial_t p_t = -\nabla \cdot (p_t v_t) + g_t p_t. \tag{3}$$

Figure 2: Illustration of our proposed VGFM, consisting of the velocity and growth flow matching deduced by the dynamic reformulation of the semi-relaxed optimal transport.

3.2 Building Unlabalnced Dynamics Based on Semi-Relaxed Optimal Transport

Though Eqs. (2) or (3) provide a formulation of unbalanced dynamics between p_0 and p_1, the equations admit a wide range of admissible dynamics. We next seek the dynamics based on semi-relaxed optimal transport. Specifically, given the semi-relaxed optimal transport

$$\min_{\pi \geq 0} \mathcal{J}_{\mathrm{sot}}(\pi) \triangleq \int_{\Omega^2} c(\mathbf{x}_0, \mathbf{x}_1)\, \mathrm{d}\pi(\mathbf{x}_0, \mathbf{x}_1) + \mathrm{KL}(\mathrm{P}^0_{\#}\pi \| p_0) \quad \text{subject to} \quad \mathrm{P}^1_{\#}\pi = p_1, \qquad (4)$$

between two unbalanced distributions p_0 and p_1, we will first present a dynamic understanding of Eq. (4) that decouples the state transition and mass growth into different periods. Based on this dynamic understanding, we will build a reasonable unbalanced dynamics between p_0 and p_1, which naturally drives our velocity and growth matching to learn the dynamics with samples (see Sect. 3.3).

Dynamic understanding of semi-relaxed optimal transport. As mentioned above, the solution of the semi-relaxed optimal transport allows both state transition and mass variation/growth. From a dynamic perspective, we understand the transport as a two-period dynamic process, in which we perform mass growth in the first period and state transition in the second period. Note that such an understanding is not practical in applications, but it provides a decoupled modeling of state transition and mass growth, which promotes a reasonable and friendly-to-matching unbalanced dynamics modeling, driving our flow matching algorithm for learning velocity and growth, as we will make clear later. More concretely, given $\lambda \in (0, 1)$, we perform mass growth controlled by g_t for $t \in [0, \lambda]$ through $\partial_t p_t = g_t p_t$ with initial and ending distributions of p_0 and p_λ respectively. For $t \in (\lambda, 1]$, the state transition controlled by v_t through $\partial_t p_t = -\nabla \cdot (p_t v_t)$ is performed with initial and ending distributions of p_λ and p_1, respectively. We then define the following two-period transport model:

$$\min_{(v_t, g_t) \in \mathcal{C}_\lambda(p_0, p_1)} \mathcal{J}^\lambda_{\mathrm{tpt}}(v_t, g_t) \triangleq (1 - \lambda) \int_\Omega \int_\lambda^1 p_t(\mathbf{x}) \| v_t(\mathbf{x}) \|^2 \mathrm{d}t \mathrm{d}\mathbf{x} + \mathcal{H}(v_t, g_t, p_t), \qquad (5)$$

where $\mathcal{H}(v_t, g_t, p_t) = \int_\Omega p_0(\mathbf{x})(e^{\int_0^\lambda g_t(\mathbf{x})\mathrm{d}t}(\int_0^\lambda g_t(\mathbf{x})\mathrm{d}t - 1) + 1)\mathrm{d}x, \mathcal{C}_\lambda(p_0, p_1) = \{(v_t, g_t) : \partial_t p_t = g_t p_t, t \in [0, \lambda]; \partial_t p_t = -\nabla \cdot (p_t v_t), t \in (\lambda, 1]\}$, and p_0 and p_1 are the given distributions. The following proposition shows the relation between the semi-relaxed optimal transport model in Eq. (4) and the two-period transport model in Eq. (5).

Proposition 1. *Assume $c(\mathbf{x}_0, \mathbf{x}_1) = \|\mathbf{x}_0 - \mathbf{x}_1\|^2$ and if we enforce $\mathrm{P}^0_{\#}\pi$ and p_0 to share the same support for admissible solution π to problem (4), then we have $\min_\pi \mathcal{J}_{\mathrm{sot}}(\pi) = \min_{v_t, g_t} \mathcal{J}^\lambda_{\mathrm{tpt}}(v_t, g_t), \forall \lambda \in (0, 1)$. Moreover, for any $\lambda \in (0, 1)$, given the optimal transport plan π^* to problem (4), let $p^*_\lambda \triangleq \mathrm{P}^0_{\#}\pi^*$, then π^* can be expressed as $\pi^* = (\mathrm{Id}, T^*)_{\#} p^*_\lambda$ where T^* is the Monge map between p^*_λ and p_1. Meanwhile, there exist a g^*_t such that $p^*_\lambda = p_0(\mathbf{x})e^{\int_0^\lambda g^*_t(\mathbf{x})\mathrm{d}t}$, and a v^*_t given by $v^*_t\left(\mathbf{x} + \frac{t-\lambda}{1-\lambda}(T^*(\mathbf{x}) - \mathbf{x})\right) = \frac{T^*(\mathbf{x})-\mathbf{x}}{1-\lambda}$, satisfying $(v^*_t, g^*_t) \in \arg\min_{v_t, g_t} \mathcal{J}^\lambda_{\mathrm{tpt}}(v_t, g_t)$.*

4

The proof is provided in the Appendix A.2. Proposition 1 indicates that problems (4) and (5) share the same optimal objective function value. Meanwhile, the optimal objective function value of the two-period transport problem (5) is independent of λ. Moreover, v_t^*, g_t^* can be constructed using π^*.

Building unbalanced dynamics. Although we have identified a scheme in which p_0 evolves into p_1 through a two-period process governed separately by v_t and g_t respectively, this decoupling does not align with the behavior observed in biological systems, where transport and growth typically occur simultaneously. To address this, we next build an unbalanced dynamics based on the dynamic understanding discussed above that allows velocity and growth to jointly drive the state transition and mass growth while ensuring consistency with the target distribution. Specifically, given v_t ($t \in (\lambda, 1]$), g_t ($t \in [0, \lambda]$) of the two-period process, we define the joint velocity $\tilde{v}_t$ and growth $\tilde{g}_t$ by

$$
\begin{aligned}
\tilde{v}_t(\mathbf{x}) &= (1 - \lambda) \cdot v_{(1-\lambda)t+\lambda}(\mathbf{x}), \\
\tilde{g}_t(\mathbf{x}) &= \lambda \cdot g_{\lambda t}\left(\psi_{\tilde{v},t}^{-1}(\mathbf{x})\right),
\end{aligned}
\tag{6}
$$

where $t \in [0, 1]$, and $\psi_{\tilde{v},t}$ is the flow generated by $\tilde{v}$, i.e., $\psi_{\tilde{v},t}(\mathbf{x}_0) = \mathbf{x}_0 + \int_0^t \tilde{v}_s(\mathbf{x})\mathrm{d}s$.

Theorem 1. *Given the initial distribution p_0, denote the ending distribution of the two-period dynamics*

$$
\partial_t p_t = g_t p_t, t \in [0, \lambda]; \quad \partial_t p_t = -\nabla \cdot (p_t v_t), t \in (\lambda, 1],
\tag{7}
$$

as p_1, and denote the ending distribution of the joint dynamics starting from p_0

$$
\partial_t \tilde{p}_t = -\nabla \cdot (\tilde{p}_t \tilde{v}_t) + \tilde{g}_t \tilde{p}_t, \quad t \in [0, 1], \quad \tilde{p}_0 = p_0,
\tag{8}
$$

as $\tilde{p}_1$, then it holds that $\tilde{p}_1 = p_1$.

The proof is detailed in Appendix A.3. Theorem 1 indicates that given the same initial distribution at $t = 0$, the two-period and the joint dynamics yield the same distribution at $t = 1$. Since $\tilde{v}_t, \tilde{g}_t$ are defined on $[0, 1]$, the joint dynamics is more practical in applications, e.g., biological systems. Meanwhile, if v_t, g_t is defined as in Proposition 1, $\tilde{v}_t, \tilde{g}_t$ will inherit the optimality properties of the semi-relaxed optimal transport, benefitting our flow matching algorithm, as shown in Sect. 3.3.

3.3 Velocity and Growth Flow Matching

Since the optimal growth function g_t^* in Proposition 1 is required to evolve p_0 to $\mathrm{P}_\#^0 \pi^*$, satisfying the marginal constraint $p_0 \exp\left(\int_0^\lambda g_s^* ds\right) = \mathrm{P}_\#^0 \pi^*$, possible choice for g_t^* is not unique. For simplicity and ease of implementation, we choose a time-independent form: $g_t^*(\mathbf{x}) = \frac{\log \mathrm{P}_\#^0 \pi^*(\mathbf{x}) - \log p_0(\mathbf{x})}{\lambda}$, which minimizes the L^2-norm energy functional of g (see Appendix A.4). By plugging the expression of v_t^* from Proposition 1 and g_t^* into Eq. (6), we obtain

$$
\tilde{v}_t(\psi_{\tilde{v},t}(\mathbf{x}_0)) = T^*(\mathbf{x}_0) - \mathbf{x}_0, \quad \tilde{g}_t(\psi_{\tilde{v},t}(\mathbf{x}_0)) = \log \mathrm{P}_\#^0 \pi^*(\mathbf{x}_0) - \log p_0(\mathbf{x}_0), \text{ where } \mathbf{x}_0 \sim p_0. \tag{9}
$$

In practice, only finite samples of p_0 and p_1 can be accessed. We then aim to learn neural networks $v_\theta(\mathbf{x}, t), g_\omega(\mathbf{x}, t)$ to approximate $\tilde{v}_t(\mathbf{x}), \tilde{g}_t(\mathbf{x})$ by velocity and growth flow matching as

$$
\min_{\theta,\omega} \mathbb{E}_{\mathbf{x}_0} \mathbb{E}_t \left[\|v_\theta(\psi_{\tilde{v},t}(\mathbf{x}_0), t) - \tilde{v}_t(\psi_{\tilde{v},t}(\mathbf{x}_0))\|^2 + |g_\omega(\psi_{\tilde{v},t}(\mathbf{x}_0), t) - \tilde{g}_t(\psi_{\tilde{v},t}(\mathbf{x}_0))|^2 \right], \tag{10}
$$

that can generalize to new samples. We first estimate π^* and T^* using samples. Given samples $\{\mathbf{x}_0^i\}_{i=1}^n$ of p_0 and $\{\mathbf{x}_0^j\}_{j=1}^m$ of p_1, We seek the optimal transport plan $\pi^{0\to1} \approx \pi^*(\mathbf{x}_0, \mathbf{x}_1)$ by solving the entropy-regularized semi-relaxed transport problem using Sinkhorn-based algorithm [50, 51] as

$$
\pi^{0\to1} = \arg\min_{\pi \geq 0} \sum_{i,j} c_{ij} \pi_{ij} + \epsilon H(\pi) + \tau \mathrm{KL}(\pi \mathbf{1}_m \| \mathbf{1}_n), \quad \text{subject to} \quad \pi^\top \mathbf{1}_n = \mathbf{1}_m, \tag{11}
$$

where $c_{ij} = \|\mathbf{x}_0^i - \mathbf{x}_1^j\|^2$, $\mathbf{1}_m$ is the all-one vector, $H(\pi)$ denotes the negative entropy of π, and ϵ and τ are hyperparameters. With $\pi^{0\to1}$, T^* can be estimated using barycentric mapping $T^*(\mathbf{x}_0^i) \approx \frac{1}{N^i} \sum_j \pi_{ij}^{0\to1} \mathbf{x}_1^j$ where $N^i = \sum_j \pi_{ij}^{0\to1}$. In implementation, for each $\mathbf{x}_0^i$, we sample j

5

from $(1, 2, \cdots, m)$ with probability $\frac{1}{N^i}\pi_{ij}^{0 \to 1}$, and approximate $T^*(\mathbf{x}_0^i) \approx \mathbf{x}_1^j$. This approximation is accurate as $\epsilon \to 0$. Therefore, $\psi_{\tilde{v}, t}(\mathbf{x}_0^i) \approx \mathbf{x}_0^i + t(\mathbf{x}_1^j - \mathbf{x}_0^i) \triangleq \mathbf{x}_t$ for $t \in [0, 1]$, and Eq. (10) becomes

$$\mathcal{L}_{\text{VGFM}}(\theta, \omega) = \sum_{i=1}^{n} \sum_{j=1}^{m} \pi_{ij}^{0 \to 1} \mathbb{E}_t \left[\left\| v_\theta(\mathbf{x}_t, t) - (\mathbf{x}_1^j - \mathbf{x}_0^i) \right\|^2 + \left| g_\omega(\mathbf{x}_t, t) - \log([\pi^{0 \to 1} \mathbf{1}_m]_i) \right|^2 \right],$$
(12)

where $[\cdot]_i$ is the i-th element. The last term in Eq. (12) is because $p_0(\mathbf{x}_0^i) = 1$, for $i = 1, \cdots, n$. In experiments, $\mathcal{L}_{\text{VGFM}}$ can be implemented using mini-batch samples. Specifically, we sample (i, j) from $\pi^{0 \to 1}$ and t from $\mathcal{U}(0, 1)$, then calculate the loss in square brackets. To improve robustness, we add a Gaussian noise to $\mathbf{x}_t$ in experiments.

3.4 Training Process

Besides the flow matching loss in Eq. (12), we also employ distribution fitting loss to improve performance further. Next, we introduce the distribution fitting loss and our training algorithm.

To achieve better performance, we incorporate the Wasserstein distance between generated samples and observed samples as part of the loss function. Specifically, let $\mathcal{X}_t = \{\mathbf{x}_t^i\}_{i=1}^{N_t}$ for $t = 0, 1, \cdots, T - 1$ denote the observed samples at different time points, and denote $p(\mathcal{X}_t) = \sum_{i=1}^{N_t} \delta_{\mathbf{x}_t^i}$. We define $\phi_{v_\theta} : \mathbb{R}^d \times \mathcal{T} \to \mathbb{R}^{d|\mathcal{T}|}$ as the trajectory mapping function parameterized by the neural network v_θ, which takes a given starting point as the initial condition and outputs particle coordinates at time indices $\mathcal{T}$ according to ODE dynamics, where $\mathcal{T}$ denotes a set of time steps. Given an initial set $\mathcal{X}_0$, the model ϕ_{v_θ} predicts particle positions at future time points in $\mathcal{T}$. Specifically, the predicted samples are computed by applying the neural ODE to $\mathcal{X}_0$ over the time indices $\{1, \cdots, T - 1\}$, i.e., $\hat{\mathcal{X}}_1, \cdots, \hat{\mathcal{X}}_{T-1} = \phi_{v_\theta}(\mathcal{X}_0, \{1, \cdots, T - 1\})$. Similarly, we define ϕ_{g_ω} as the particle weight mapping function parameterized by the neural network g_ω, which takes the initial weight of particle i as input and outputs the corresponding weight values at $\mathcal{T}$ under ODE dynamics. For simplicity of notation, we use $\hat{w}(\hat{\mathbf{x}})$ for $\hat{\mathbf{x}} \in \hat{\mathcal{X}}_t$ to denote the weight generated by ϕ_{g_ω} corresponding to the particles in set $\hat{\mathcal{X}}$ which is generated by ϕ_{v_θ}. The distribution fitting loss is defined as the Wasserstein distance as

$$\mathcal{L}_{\text{OT}}(\theta, \omega) = \sum_{t=1}^{T-1} \mathcal{W}_1 \left(\frac{1}{N_t} p(\mathcal{X}_t), \frac{1}{\sum_{\hat{\mathbf{x}} \in \hat{\mathcal{X}}_t} \hat{w}(\hat{\mathbf{x}})} p_{\hat{w}}(\hat{\mathcal{X}}_t) \right),$$
(13)

where $p_{\hat{w}}(\hat{\mathcal{X}}_t) = \sum_{\hat{\mathbf{x}} \in \hat{\mathcal{X}}_t} \hat{w}(\hat{\mathbf{x}})\delta_{\hat{\mathbf{x}}}$, $\mathcal{W}_1$ is the 1-Wasserstein distance with Euclidean norm.

Total loss and algorithm. Note that the matching loss can be easily generalized to multi-time snapshots by employing Eq. (12) among two consecutive snapshots p_t and p_{t+1}. Combined with distribution fitting loss in Eq. (13), we obtain the final loss

$$\mathcal{L}(\theta, \omega) = \mathcal{L}_{\text{VGFM}}(\theta, \omega) + \mathcal{L}_{\text{OT}}(\theta, \omega)$$
(14)

During training, we employ a parameter scheduling scheme in which we initially use $\mathcal{L}_{\text{VGFM}}$ as a warm-up stage, before enabling both loss terms for joint training. This design provides a notable advantage: after the warm-up stage, v_θ and g_ω are well-initialized through conditional matching, which facilitates convergence when switching to $\mathcal{W}_1$-based training. The detailed algorithm is presented in Algorithm 1. For further details on the warm-up procedure and parameter scheduling, please refer to Appendix B.1.

4 Experiments

We evaluate VGFM on synthetic and real datasets, and compare it with state-of-the-art approaches, including methods that account for distributional unbalancedness [25, 43, 49] as well as those that assume mass conservation [21, 36, 39]. Our code will be released online.

Synthetic datasets. Inspired by [22, 25], we adopt the Simulation Gene dataset that applies a three-gene regulatory network to produce a quiescent region and an area exhibiting both transition and growth that can be observed. We also use Dyngen [52] to simulate a scRNA-seq dataset from a dynamic cellular process, which exhibits pronounced branching unbalancedness, with significantly

Algorithm 1: Training algorithm of joint velocity-growth flow matching

---

Input: Observed data $\mathcal{X}_0, \ldots, \mathcal{X}_{T-1}$; warm-up epochs M_1; training epochs M_2
Output: Trained velocity field v_θ and growth function g_ω
Compute transport plans $\pi^{t \to t+1}$ for $t = 0, \ldots, T-2$;
for $i = 1$ **to** M_2 **do**
    for $t_0 = 0$ **to** $T-2$ **do**
        Sample a batch $(i, j) \sim \pi^{t_0 \to t_0+1}$;
        Sample $t \sim \mathcal{U}(0, 1) + t_0$, and $\mathbf{x}_t \sim \mathcal{N}(t\mathbf{x}_1^j + (1-t)\mathbf{x}_0^i, \sigma^2 I)$;
        $\mathcal{L} \leftarrow \mathcal{L} + \left\| v_\theta(\mathbf{x}_t, t) - (\mathbf{x}_1^j - \mathbf{x}_0^i) \right\|^2 + \left| g_\omega(\mathbf{x}_t, t) - \log([\pi^{0 \to 1} \mathbf{1}_m]_i) \right|^2$;
        if $i > M_1$ **then**
            $\hat{\mathcal{X}}_{t_0+1} \leftarrow \phi_{v_\theta}(\hat{\mathcal{X}}_{t_0}, t_0 + 1), \quad \hat{w}_{t_0+1}(\hat{\mathcal{X}}_{t_0+1}) \leftarrow \phi_{g_\omega}(\hat{\mathcal{X}}_{t_0}, t_0 + 1)$;
            $\mathcal{L} \leftarrow \mathcal{L} + \mathcal{W}_1 \left(\frac{1}{N_{t_0+1}} p(\mathcal{X}_{t_0+1}), \frac{1}{\sum_{\hat{\mathbf{x}} \in \hat{\mathcal{X}}_t} \hat{w}(\hat{\mathbf{x}})} p_{\hat{w}}(\hat{\mathcal{X}}_{t_0+1}) \right)$;
    Update θ, ω using $\mathcal{L}$

---

different cell abundances across divergent lineages. Following the experiment setup of [30], we use PHATE [53] to reduce its dimensions to 5. Additionally, inspired by [25] that employs a high-dimensional Gaussian mixture model [54] to evaluate the scalability of models, we adopt a more challenging setting: 1000-dimensional Gaussian mixtures.

Real-world dataset. We conduct experiments on two real-world datasets, Embryoid Body (EB) [55] and CITE-seq (CITE) [56], both preprocessed following the procedures in [17, 21]. Each dataset is evaluated under both 5- and 50-dimensional PCA projections. Specifically, the EB (5D), CITE (5D), and CITE (50D) configurations are assessed using a hold-out strategy, same as [36], in which an intermediate time point is excluded during training. The model is then used to predict the distribution at the hold-out time, and we compute the $\mathcal{W}_1$ distance between the predicted and true distributions at that time point. The EB (50D) setting is further used for comparison against [25], evaluated using both $\mathcal{W}_1$ and the Relative Mass Error (RME) (see below).

Evaluation metrics. We follow [25] to use $\mathcal{W}_1$ to measure the distance between the predicted cell distribution and the true cell distribution. Additionally, to assess the accuracy of the growth function g_ω, we normalize the total mass at time 0 to 1, and denote the relative mass at time t *w.r.t* time 0 as m_t, *i.e.*, $m_t = \frac{N_t}{N_0}$. The predicted relative mass at time t based on the evolution induced by g_ω is denoted as $\hat{m}_t = \sum_{\hat{\mathbf{x}} \in \hat{\mathcal{X}}_t} \hat{w}(\hat{\mathbf{x}})/N_0$, where $\sum_{\hat{\mathbf{x}} \in \hat{\mathcal{X}}_t} \hat{w}(\hat{\mathbf{x}})$ is the predicted total mass at time t. We define the relative mass error, denoted as RME, *i.e.*, $\text{RME} = \frac{|m_t - \hat{m}_t|}{m_t}$.

Inplementation details. We employ a 3-layer (5-layer for dimensions greater than 50) MLP with 256 hidden units and LeakyReLU activation to parameterize both the velocity field v_θ and the growth function g_ω. Optimization is performed using the Adam optimizer with a learning rate of 10^{-4}. A warm-up stage of 200-800 iterations is applied (only matching loss in Eq. (12)), after which the distribution fitting loss $\mathcal{L}_{\text{OT}}$ defined in Eq. (13) is applied for an additional 30 training epochs. We will discuss the strategy to set ϵ and τ in the Appendix B.1.

4.1 Results and Analysis

Ability to reconstruct cellular dynamics. As shown in Tab. 1, our model achieves lowest mean $\mathcal{W}_1$ and RME on synthetic datasets, outperforming both unbalancedness-aware methods [22, 25, 49] and unbalancedness-ignoring methods [21, 36], which demonstrate the ability of VGFM to model cellular dynamics for data and mass fitting. We also visualize the learned trajectory and growth function on the Simulation Gene dataset in Figs. 3 (a-c). Figures 3 (a-c) show that VGFM not only reconstructs accurate trajectories but also produces faithful predictions of spatially varying growth rates.

Scalability and mass-matching performance compared with existing unbalanced models. While existing SOTA approaches of UDSB [49], TIGON [22] and DeepRUOT [25] incorporate unbalanced modeling, these models either introduce biologically implausible transitions [49] (as discussed in [25]) or face difficulties in scaling to high-dimensions [22, 25, 49]. As a result, these methods do not

(a) Predicted dynamics   (b) Predicted growth rate   (c) True growth rate

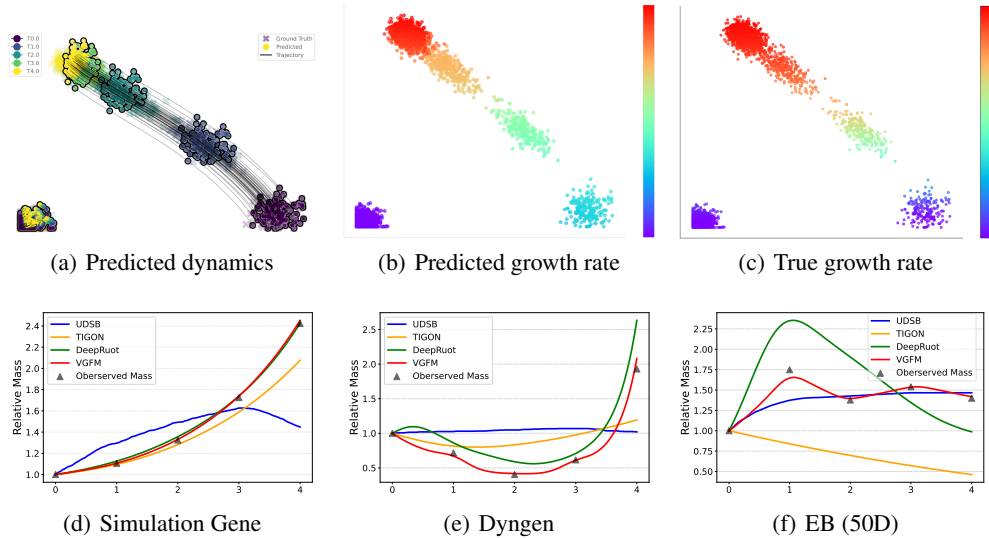(d) Simulation Gene   (e) Dyngen   (f) EB (50D)

Figure 3: (a) Predicted dynamics with trajectories of VGFM on Simulation Gene. (b) Predicted and (c) true growth rates on Simulation Gene. Note that for Simulation Gene, the true growth rates could be accessed. (d), (e) and (f) respectively compare predicted relative mass by UDSB, TIGON, DeepRUOT, and VFGM, and observed relative mass from data, on three datasets. Note that in (f), on 50D dataset, the mass predicted by TIGON deviates significantly from the observed trend, because of its difficulty in handling high-dimensional data as discussed in their paper [22].

Table 1: Mean $\mathcal{W}_1$ and RME over all time on synthetic datasets. *OT-CFM and OT-MFM do not model the growth function, thus, RME is not computed. "N/C" means "not converge".

Method	Simulation Gene (2D)		Dyngen (5D)		Gaussian (1000D)	
	$\mathcal{W}_1$	RME	$\mathcal{W}_1$	RME	$\mathcal{W}_1$	RME
OT-CFM* [21]	0.302	—	3.926	—	10.126	—
OT-MFM* [36]	0.311	—	3.976	—	11.008	—
UDSB [49]	0.665	0.192	1.914	0.658	25.304	0.965
TIGON [22]	0.099	0.065	1.029	0.542	N/C	N/C
DeepRUOT [25]	0.068	0.016	0.474	0.199	N/C	N/C
VGFM	**0.046**	**0.006**	**0.420**	**0.053**	**3.010**	**0.037**

perform well or converge on the 1000-dimensional Gaussian dataset, as in Tab. 1. In contrast, VGFM integrates flow matching based on unbalanced transport, allowing it to scale more effectively to high-dimensional datasets. Our method more accurately recovers the ground-truth dynamics defined in [25] and achieves superior mass-matching accuracy, as shown in Tab. 1 and Figs. 3 (d-f).

Hold-one-out results on real-world datasets. Table 2 compares hold-one-out results of different methods on EB (5D) and CITE (5D and 50D) datasets. It can be observed that VGFM outperforms most existing approaches in terms of $\mathcal{W}_1$ distance. We attribute this to the integration of complementary strengths from both flow matching and simulation-based (Neural ODE) frameworks. On the one hand, flow matching provides a robust initialization for learning the velocity field and growth rate, which helps maintain training stability after incorporating the distribution fitting loss $\mathcal{L}_{OT}$, leading to better performance than purely simulation-based models, as also shown in Fig. 4. On the other hand, since the flow matching objective serves only as an upper bound on the true Wasserstein distance [57], the introduction of $\mathcal{L}_{OT}$ allows direct optimization of the distribution fitting loss, further enhancing model performance. Moreover, by explicitly modeling cell growth through a time-varying weight function, our framework generalizes beyond the conventional setting where Wasserstein distance is computed between unweighted discrete measures, thereby offering greater flexibility in evaluation and enabling more possible transport solutions.

Ablation study on loss terms. To assess the contribution of each loss component in our framework, we perform an ablation study on the EB dataset with unwhitened 50-dimensional PCA features. Table 3 reports the performance across four time points. VGFM in general achieves the lowest $\mathcal{W}_1$ and RME values (excluding time 1) compared with VGFM (w/o $\mathcal{L}_{\text{OT}}$) and VGFM (w/o $\mathcal{L}_{\text{VGFM}}$), demonstrating the effectiveness of both our joint velocity-growth matching loss and distribution fitting loss. Notably, by removing $\mathcal{L}_{\text{VGFM}}$, both $\mathcal{W}_1$ and RME increase by a significant margin, implying the importance of our velocity and growth matching to our framework. Consistent with our motivation in Sect. 3.4, adding in distribution fitting loss $\mathcal{L}_{\text{OT}}$ results in lower $\mathcal{W}_1$ and RME, improved fitting ability to observed distributions.

Table 2: Mean hold-one-out results on EB and CITE datasets over hold-out times.

Method	EB	CITE	
	5D	5D	50D
OT-CFM [21]	0.790	0.882	38.756
SF^{2}M [39]	0.793	0.920	38.524
WLF-UOT [43]	0.738	0.733	37.007
UDSB [49]	1.206	2.023	44.168
OT-MFM [36]	0.713	0.724	36.394
DeepRUOT [25]	0.774	**0.648**	35.539
VGFM	**0.676**	0.650	**34.182**

(a) Predicted dynamics (w/o $\mathcal{L}_{\text{OT}}$)   (b) Predicted dynamics   (c) Predicted growth rate
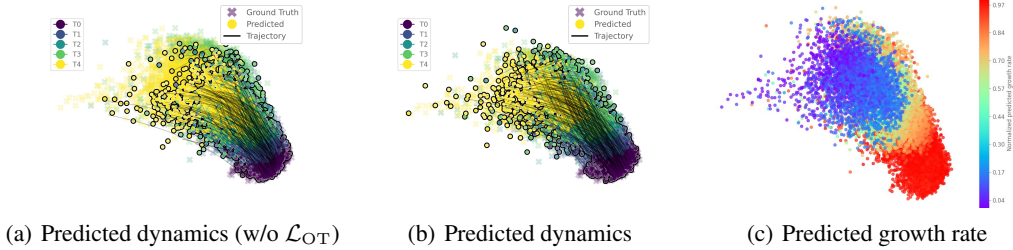
Figure 4: Visualization of predicted dynamics by (a) VFGM (w/o $\mathcal{L}_{\text{OT}}$) and (b) VGFM, and growth rate by (c) VFGM, on EB (5D) dataset, where the hold-out time is the first intermediate timepoint.

Comparison on computational efficiency. We compare the computational cost of our method and the SOTA method DeepRUOT [25] in Tab. 3. For fair comparison, all methods in Tab. 3 adopt the same networks 5-layer MLP with 256 hidden units, and are trained on the same GPU until convergence. As shown in Table 3, our full model requires slightly more training time than the variant using only $\mathcal{L}_{\text{VGFM}}$, due to the training with additional distribution fitting loss. However, it still achieves faster convergence compared with simulation-based methods of DeepRUOT [25] and the ablation variant without $\mathcal{L}_{\text{VGFM}}$. This demonstrates the critical role of the loss $\mathcal{L}_{\text{VGFM}}$ for facilitating training convergence.

Table 3: Ablation study on EB (50D) dataset. For comparison, we also report the results of the SOTA approach DeepRUOT [25] in this table.

Method	t_1		t_2		t_3		t_4		Training time
	$\mathcal{W}_1$	RME	$\mathcal{W}_1$	RME	$\mathcal{W}_1$	RME	$\mathcal{W}_1$	RME	
DeepRUOT [25]	8.169	0.416	9.041	0.415	9.348	0.119	9.808	0.296	90 (mins)
VGFM (w/o $\mathcal{L}_{\text{OT}}$)	8.915	**0.020**	10.590	0.098	10.915	0.067	11.635	0.088	6 (mins)
VGFM (w/o $\mathcal{L}_{\text{VGFM}}$)	8.644	0.650	10.167	0.710	11.052	0.823	11.530	0.862	62 (mins)
VGFM	**7.951**	0.089	**8.747**	**0.042**	**9.244**	**0.019**	**9.620**	**0.044**	13 (mins)

5   Conclusion, Limitation, and Future Work

The paper proposes the joint Velocity-Growth Flow Matching (VGFM) method that jointly learns state transition and mass growth of single-cell populations via flow matching. VGFM designs an ideal dynamics containing a velocity field and a growth function, driven by our presented two-period dynamic understanding of the static semi-relaxed optimal transport model. Approximating the ideal

dynamics using neural networks yields the velocity-growth joint flow matching framework. Extensive experiments on both synthetic and real datasets demonstrate the effectiveness of our method.

Although our approach achieves better scalability and training efficiency compared to simulation-based methods, it is not entirely simulation-free due to the incorporation of the distribution fitting loss $\mathcal{L}_{\mathrm{OT}}$. Moreover, since the learned growth rate relies on the observed cell counts at each time point, it may inadvertently capture effects that are not solely attributable to biological growth. Future work could address them by integrating biological priors into the learning process of the growth function g, and by exploring fully simulation-free alternatives that can achieve comparable performance.

References

[1] V Gontis, J Ruseckas, and A Kononovičius. A long-range memory stochastic model of the return in financial markets. *Physica A: Statistical Mechanics and its Applications*, 389(1):100–106, 2010.

[2] Christian LE Franzke, Terence J O'Kane, Judith Berner, Paul D Williams, and Valerio Lucarini. Stochastic climate theory and modeling. *Wiley Interdisciplinary Reviews: Climate Change*, 6(1):63–78, 2015.

[3] Grace Hui Ting Yeo, Sachit D Saksena, and David K Gifford. Generative modeling of single-cell time series with prescient enables prediction of cell trajectories with interventions. *Nature Communications*, 12(1):3222, 2021.

[4] Geoffrey Schiebinger, Jian Shu, Marcin Tabaka, Brian Cleary, Vidya Subramanian, Aryeh Solomon, Joshua Gould, Siyan Liu, Stacie Lin, Peter Berube, et al. Optimal-transport analysis of single-cell gene expression identifies developmental trajectories in reprogramming. *Cell*, 176(4):928–943, 2019.

[5] Stephen Zhang, Anton Afanassiev, Laura Greenstreet, Tetsuya Matsumoto, and Geoffrey Schiebinger. Optimal transport analysis reveals trajectories in steady-state systems. *PLoS Computational Biology*, 17(12):e1009466, 2021.

[6] Conrad H Waddington. Canalization of development and the inheritance of acquired characters. *Nature*, 150(3811):563–565, 1942.

[7] Charlotte Bunne, Stefan G Stark, Gabriele Gut, Jacobo Sarabia Del Castillo, Mitch Levesque, Kjong-Van Lehmann, Lucas Pelkmans, Andreas Krause, and Gunnar Rätsch. Learning single-cell perturbation responses using neural optimal transport. *Nature Methods*, 20(11):1759–1768, 2023.

[8] James A Hay, Lee Kennedy-Shaffer, Sanjat Kanjilal, Niall J Lennon, Stacey B Gabriel, Marc Lipsitch, and Michael J Mina. Estimating epidemiologic dynamics from cross-sectional viral load distributions. *Science*, 373(6552):eabh0635, 2021.

[9] Jim Oeppen and James W Vaupel. Broken limits to life expectancy. *Science*, 296(5570):1029–1031, 2002.

[10] Zhenyi Zhang, Yuhao Sun, Qiangwei Peng, Tiejun Li, and Peijie Zhou. Integrating dynamical systems modeling with spatiotemporal scrna-seq data analysis. *Entropy*, 27(5), 2025.

[11] Evan Z Macosko, Anindita Basu, Rahul Satija, James Nemesh, Karthik Shekhar, Melissa Goldman, Itay Tirosh, Allison R Bialas, Nolan Kamitaki, Emily M Martersteck, et al. Highly parallel genome-wide expression profiling of individual cells using nanoliter droplets. *Cell*, 161(5):1202–1214, 2015.

[12] Allon M Klein, Linas Mazutis, Ilke Akartuna, Naren Tallapragada, Adrian Veres, Victor Li, Leonid Peshkin, David A Weitz, and Marc W Kirschner. Droplet barcoding for single-cell transcriptomics applied to embryonic stem cells. *Cell*, 161(5):1187–1201, 2015.

[13] Dragomirka Jovic, Xue Liang, Hua Zeng, Lin Lin, Fengping Xu, and Yonglun Luo. Single-cell rna sequencing technologies and applications: A brief overview. *Clinical and Translational Medicine*, 12(3):e694, 2022.

[14] Antoine-Emmanuel Saliba, Alexander J Westermann, Stanislaw A Gorski, and Jörg Vogel. Single-cell rna-seq: advances and future challenges. *Nucleic Acids Research*, 42(14):8845–8860, 2014.

[15] Ashraful Haque, Jessica Engel, Sarah A Teichmann, and Tapio Lönnberg. A practical guide to single-cell rna-sequencing for biomedical research and clinical applications. *Genome Medicine*, 9:1–12, 2017.

[16] David Lähnemann, Johannes Köster, Ewa Szczurek, Davis J McCarthy, Stephanie C Hicks, Mark D Robinson, Catalina A Vallejos, Kieran R Campbell, Niko Beerenwinkel, Ahmed Mahfouz, et al. Eleven grand challenges in single-cell data science. *Genome Biology*, 21:1–35, 2020.

[17] Alexander Tong, Jessie Huang, Guy Wolf, David Van Dijk, and Smita Krishnaswamy. Trajectorynet: A dynamic optimal transport network for modeling cellular dynamics. In *ICML*, 2020.

[18] Charlotte Bunne, Laetitia Papaxanthos, Andreas Krause, and Marco Cuturi. Proximal optimal transport modeling of population dynamics. In *AISTATS*, 2022.

[19] Takeshi Koshizuka and Issei Sato. Neural lagrangian schrödinger bridge: Diffusion modeling for population dynamics. In *ICLR*, 2023.

[20] Tianrong Chen, Guan-Horng Liu, Molei Tao, and Evangelos Theodorou. Deep momentum multi-marginal schrödinger bridge. In *NeurIPS*, 2023.

[21] Alexander Tong, Kilian Fatras, Nikolay Malkin, Guillaume Huguet, Yanlei Zhang, Jarrid Rector-Brooks, Guy Wolf, and Yoshua Bengio. Improving and generalizing flow-based generative models with minibatch optimal transport. *Transactions on Machine Learning Research*, pages 1–34, 2024.

[22] Yutong Sha, Yuchi Qiu, Peijie Zhou, and Qing Nie. Reconstructing growth and dynamic trajectories from single-cell transcriptomics data. *Nature Machine Intelligence*, 6(1):25–39, 2024.

[23] Qi Jiang and Lin Wan. A physics-informed neural sde network for learning cellular dynamics from time-series scrna-seq data. *Bioinformatics*, 40:ii120–ii127, 2024.

[24] Antonio Terpin, Nicolas Lanzetti, Martín Gadea, and Florian Dorfler. Learning diffusion at lightspeed. In *NeurIPS*, 2024.

[25] Zhenyi Zhang, Tiejun Li, and Peijie Zhou. Learning stochastic dynamics from snapshots through regularized unbalanced optimal transport. In *ICLR*, 2025.

[26] Xi Zhang, Yuan Pu, Yuki Kawamura, Andrew Loza, Yoshua Bengio, Dennis Shung, and Alexander Tong. Trajectory flow matching with applications to clinical time series modelling. In *NeurIPS*, 2024.

[27] Anming Gu, Edward Chien, and Kristjan Greenewald. Partially observed trajectory inference using optimal transport and a dynamics prior. In *ICLR*, 2025.

[28] Martin Rohbeck, Charlotte Bunne, Edward De Brouwer, Jan-Christian Huetter, Anne Biton, Kelvin Y. Chen, Aviv Regev, and Romain Lopez. Modeling complex system dynamics with flow matching across time and conditions. In *ICLR*, 2025.

[29] Ricky T. Q. Chen, Yulia Rubanova, Jesse Bettencourt, and David K Duvenaud. Neural ordinary differential equations. In *NeurIPS*, 2018.

[30] Guillaume Huguet, Daniel Sumner Magruder, Alexander Tong, Oluwadamilola Fasina, Manik Kuchroo, Guy Wolf, and Smita Krishnaswamy. Manifold interpolating optimal-transport flows for trajectory inference. In *NeurIPS*, 2022.

[31] Yaron Lipman, Ricky TQ Chen, Heli Ben-Hamu, Maximilian Nickel, and Matthew Le. Flow matching for generative modeling. In *ICLR*, 2023.

[32] Xingchao Liu, Chengyue Gong, and qiang liu. Flow straight and fast: Learning to generate and transfer data with rectified flow. In *ICLR*, 2023.

[33] Michael S Albergo and Eric Vanden-Eijnden. Building normalizing flows with stochastic interpolants. In *ICLR*, 2023.

[34] Aram-Alexandre Pooladian, Heli Ben-Hamu, Carles Domingo-Enrich, Brandon Amos, Yaron Lipman, and Ricky TQ Chen. Multisample flow matching: Straightening flows with minibatch couplings. In *ICLR*, 2023.

[35] Luca Eyring, Dominik Klein, Théo Uscidda, Giovanni Palla, Niki Kilbertus, Zeynep Akata, and Fabian J Theis. Unbalancedness in neural monge maps improves unpaired domain translation. In *ICLR*, 2024.

[36] Kacper Kapusniak, Peter Potaptchik, Teodora Reu, Leo Zhang, Alexander Tong, Michael Bronstein, Joey Bose, and Francesco Di Giovanni. Metric flow matching for smooth interpolations on the data manifold. In *NeurIPS*, 2024.

[37] Lazar Atanackovic, Xi Zhang, Brandon Amos, Mathieu Blanchette, Leo J Lee, Yoshua Bengio, Alexander Tong, and Kirill Neklyudov. Meta flow matching: Integrating vector fields on the wasserstein manifold. In *ICML 2024 Workshop on Geometry-grounded Representation Learning and Generative Modeling*, 2024.

[38] Dominik Klein, Théo Uscidda, Fabian J Theis, and marco cuturi. GENOT: Entropic (gromov) wasserstein flow matching with applications to single-cell genomics. In *NeurIPS*, 2024.

[39] Alexander Y Tong, Nikolay Malkin, Kilian Fatras, Lazar Atanackovic, Yanlei Zhang, Guillaume Huguet, Guy Wolf, and Yoshua Bengio. Simulation-free schrödinger bridges via score and flow matching. In *AISTATS*, 2024.

[40] Gabriele Corso, Vignesh Ram Somnath, Noah Getz, Regina Barzilay, Tommi Jaakkola, and Andreas Krause. Composing unbalanced flows for flexible docking and relaxation. In *ICLR*, 2025.

[41] Alessandro Palma, Till Richter, Hanyi Zhang, Manuel Lubetzki, Alexander Tong, Andrea Dittadi, and Fabian J Theis. Multi-modal and multi-attribute generation of single cells with cfgen. In *ICLR*, 2025.

[42] Kirill Neklyudov, Rob Brekelmans, Daniel Severo, and Alireza Makhzani. Action matching: Learning stochastic dynamics from samples. In *ICML*, 2023.

[43] Kirill Neklyudov, Rob Brekelmans, Alexander Tong, Lazar Atanackovic, qiang liu, and Alireza Makhzani. A computational framework for solving wasserstein lagrangian flows. In *ICML*, 2024.

[44] Lenaic Chizat, Gabriel Peyré, Bernhard Schmitzer, and François-Xavier Vialard. Unbalanced optimal transport: Dynamic and kantorovich formulations. *Journal of Functional Analysis*, 274(11):3090–3123, 2018.

[45] Matthias Liero, Alexander Mielke, and Giuseppe Savaré. Optimal entropy-transport problems and a new hellinger–kantorovich distance between positive measures. *Inventiones Mathematicae*, 211(3):969–1117, 2018.

[46] Leonid V Kantorovich. On the translocation of masses. In *Dokl. Akad. Nauk. USSR (NS)*, 1942.

[47] Yann Brenier. Décomposition polaire et réarrangement monotone des champs de vecteurs. *CR Acad. Sci. Paris Sér. I Math.*, 305:805–808, 1987.

[48] Jaemoo Choi and Jaewoong Choi. Scalable simulation-free entropic unbalanced optimal transport. *arXiv preprint arXiv:2410.02656*, 2024.

[49] Matteo Pariset, Ya-Ping Hsieh, Charlotte Bunne, Andreas Krause, and Valentin De Bortoli. Unbalanced diffusion schrödinger bridge. *arXiv preprint arXiv:2306.09099*, 2023.

[50] Marco Cuturi. Sinkhorn distances: Lightspeed computation of optimal transport. In *NeurIPS*, 2013.

[51] Gabriel Peyré, Marco Cuturi, et al. Computational optimal transport: With applications to data science. *Foundations and Trends® in Machine Learning*, 11(5-6):355–607, 2019.

[52] Robrecht Cannoodt, Wouter Saelens, Louise Deconinck, and Yvan Saeys. Spearheading future omics analyses using dyngen, a multi-modal simulator of single cells. *Nature Communications*, 12(1):3942, 2021.

[53] Kevin R Moon, David Van Dijk, Zheng Wang, Scott Gigante, Daniel B Burkhardt, William S Chen, Kristina Yim, Antonia van den Elzen, Matthew J Hirn, Ronald R Coifman, et al. Visualizing structure and transitions in high-dimensional biological data. *Nature Biotechnology*, 37(12):1482–1492, 2019.

[54] Lars Ruthotto, Stanley J Osher, Wuchen Li, Levon Nurbekyan, and Samy Wu Fung. A machine learning framework for solving high-dimensional mean field game and mean field control problems. *Proceedings of the National Academy of Sciences*, 117(17):9183–9193, 2020.

[55] Kevin R Moon, Jay S Stanley III, Daniel Burkhardt, David van Dijk, Guy Wolf, and Smita Krishnaswamy. Manifold learning-based methods for analyzing single-cell rna-sequencing data. *Current Opinion in Systems Biology*, 7:36–46, 2018.

[56] Christopher Lance, Malte D Luecken, Daniel B Burkhardt, Robrecht Cannoodt, Pia Rautenstrauch, Anna Laddach, Aidyn Ubingazhibov, Zhi-Jie Cao, Kaiwen Deng, Sumeer Khan, et al. Multimodal single cell data integration challenge: results and lessons learned. *BioRxiv*, pages 2022–04, 2022.

[57] Joe Benton, George Deligiannidis, and Arnaud Doucet. Error bounds for flow matching methods. *Transactions on Machine Learning Research*, 2024.

[58] Jean-David Benamou and Yann Brenier. A computational fluid mechanics solution to the monge-kantorovich mass transfer problem. *Numerische Mathematik*, 84(3):375–393, 2000.

[59] Alessio Figalli and Federico Glaudo. *An invitation to optimal transport, Wasserstein distances, and gradient flows*. EMS Press, 2021.

[60] Caleb Weinreb, Alejo Rodriguez-Fraticelli, Fernando D Camargo, and Allon M Klein. Lineage tracing on transcriptional landscapes links state to fate during differentiation. *Science*, 367(6479):eaaw3381, 2020.

Outline of Appendix

The appendix is organized into three main parts.

Appendix A presents the theoretical foundations. We begin by reviewing the Brenier–Benamou theorem [58], followed by detailed proofs of Proposition 1 and Theorem 1 that are stated in the main text, as well as the justification for our choice of the reparameterized growth function $\tilde{g}$ in Eq. (9).

Appendix B focuses on experiments. We first describe our general implementation setup, including the strategy for selecting the hyperparameters in Eq. (11). Next, we provide detailed settings, visualizations and analysis for each experiment.

Appendix C discusses the broader impacts of our work.

A Proofs

A.1 Background: Brenier-Benamou Formulation

We first recall the dynamic formulation of balanced optimal transport, which is known as Brenier-Benamou formula [58]. In this paper, we assume p_0 and p_1 are absolutely continuous *w.r.t.* Lebesgue measure, which is omitted for convenience of description.

Theorem A-2 (Brenier-Benamou formula). *Given two probability measures $p_0, p_1 \in \mathcal{P}_2(\Omega)$, it holds that*

$$\mathcal{W}_2^2(p_0, p_1) = \inf_{\rho_t, v_t} \left\{ \int_0^1 \int_\Omega \|v_t(\mathbf{x})\|^2 \mathrm{d}\mathbf{x}\mathrm{d}t \Big| \partial_t p_t = -\nabla \cdot (p_t v_t),\ p_{t=0} = p_0, p_{t=1} = p_1 \right\} \quad \text{(A-15)}$$

and the optimal $v_t^*(\mathbf{x})$ can be expressed by Monge map between p_0 and p_1. i.e.,

$$v_t(\mathbf{x} + t(T^*(\mathbf{x}) - \mathbf{x})) = T^*(\mathbf{x}) - \mathbf{x},\ \mathbf{x} \sim p_0 \quad \text{(A-16)}$$

A.2 Proof of Proposition 1

For the convenience of reading, here we restate Proposition 1 in the main text as Proposition A-2.

Proposition A-2. *Assume $c(\mathbf{x}_0, \mathbf{x}_1) = \|\mathbf{x}_0 - \mathbf{x}_1\|^2$ and if we enforce $\mathrm{P}_\#^0 \pi$ and p_0 to share the same support for admissible solution π to problem (4), then we have $\min_\pi \mathcal{J}_{\mathrm{sot}}(\pi) = \min_{v_t, g_t} \mathcal{J}_{\mathrm{tpt}}^\lambda(v_t, g_t), \forall \lambda \in (0, 1)$. Moreover, for any $\lambda \in (0, 1)$, given the optimal transport plan π^* to problem (4), let $p_\lambda^* \triangleq \mathrm{P}_\#^0 \pi^*$, then π^* can be expressed as $\pi^* = (\mathrm{Id}, T^*)_\# p_\lambda^*$ where T^* is the Monge map between p_λ^* and p_1. Meanwhile, there exist a g_t^* such that $p_\lambda^* = p_0(\mathbf{x})e^{\int_0^\lambda g_t^*(\mathbf{x})\mathrm{d}t}$, and a v_t^* given by*

$$v_t^* \left(\mathbf{x} + \frac{t - \lambda}{1 - \lambda}(T^*(\mathbf{x}) - \mathbf{x}) \right) = \frac{T^*(\mathbf{x}) - \mathbf{x}}{1 - \lambda}, \quad \text{(A-17)}$$

satisfying $(v_t^*, g_t^*) \in \arg\min_{v_t, g_t} \mathcal{J}_{\mathrm{tpt}}^\lambda(v_t, g_t)$.

Proof. Recall that when $c(\mathbf{x}_0, \mathbf{x}_1) = \|\mathbf{x}_0 - \mathbf{x}_1\|^2$, problems (4) and (5) are respectively

$$\min_{\pi \geq 0} \mathcal{J}_{\mathrm{sot}}(\pi) \triangleq \int_{\Omega^2} \|\mathbf{x}_0 - \mathbf{x}_1\|^2\ \mathrm{d}\pi(\mathbf{x}_0, \mathbf{x}_1) + \mathrm{KL}(\mathrm{P}_\#^0 \pi \| p_0) \quad \text{subject to} \quad \mathrm{P}_\#^1 \pi = p_1,$$

and

$$\min_{(v_t, g_t) \in \mathcal{C}_\lambda(p_0, p_1)} \mathcal{J}_{\mathrm{tpt}}^\lambda(v_t, g_t) \triangleq (1 - \lambda) \int_\Omega \int_\lambda^1 p_t(\mathbf{x})\|v_t(\mathbf{x})\|^2 \mathrm{d}t\mathrm{d}x + \mathcal{H}(v_t, g_t, p_t),$$

where $\mathcal{H}(v_t, g_t, p_t) = \int_\Omega p_0(\mathbf{x})(e^{\int_0^\lambda g_t(\mathbf{x})\mathrm{d}t}(\int_0^\lambda g_t(\mathbf{x})\mathrm{d}t - 1) + 1)\mathrm{d}x, \mathcal{C}_\lambda(p_0, p_1) = \{(v_t, g_t) : \partial_t p_t = g_t p_t, t \in [0, \lambda]; \partial_t p_t = -\nabla \cdot (p_t v_t), t \in (\lambda, 1]\}$

(1) We first prove $\min_\pi \mathcal{J}_{\mathrm{sot}}(\pi) \geq \min_{v_t, g_t} \mathcal{J}_{\mathrm{tpt}}^\lambda(v_t, g_t)$.

14

Let π^* be the optimal solution to problem (4). For any $\lambda \in (0,1)$, define $p_\lambda = \mathrm{P}^0_{\#}\pi^*$, and let $w_\lambda(\mathbf{x}) := \frac{p_\lambda(\mathbf{x})}{p_0(\mathbf{x})}$. Define the growth as

$$\frac{\mathrm{d}}{\mathrm{d}t}\log w_t(\mathbf{x}) = g_t(\mathbf{x}), t \in [0, \lambda].$$

This implies the continuity equation $\partial_t p_t = g_t p_t$ for $t \in [0, \lambda]$, and hence we have $p_0(\mathbf{x})\exp\left(\int_0^\lambda g_t(\mathbf{x})dt\right) = \mathrm{P}^0_{\#}\pi^*$.

By Brenier's theorem [51], we have $\pi^* = (\mathrm{Id}, T^*)_{\#}p_\lambda$, where $T^*(\mathbf{x})$ is the Monge map from p_λ to p_1. Define

$$g_t(\mathbf{x}) = \frac{\log p_\lambda(\mathbf{x}) - \log p_0(\mathbf{x})}{\lambda}, \quad v_t\left(\mathbf{x} + \frac{t-\lambda}{1-\lambda}(T^*(\mathbf{x}) - \mathbf{x})\right) = \frac{T^*(\mathbf{x}) - \mathbf{x}}{1-\lambda}. \tag{A-18}$$

Plugging into the dynamic objective and using the definition of KL-divergence:

$$\mathrm{KL}(p_\lambda \| p_0) = \int_\Omega p_0(\mathbf{x})\left(\frac{p_\lambda(\mathbf{x})}{p_0(\mathbf{x})}\left(\log\frac{p_\lambda(\mathbf{x})}{p_0(\mathbf{x})} - 1\right) + 1\right)\mathrm{d}\mathbf{x},$$

we obtain

$$\mathcal{J}^\lambda_{\mathrm{tpt}}(v_t, g_t) = \int_\Omega p_0(\mathbf{x})\left(e^{\int_0^\lambda g_t(\mathbf{x})\mathrm{d}t}\left(\int_0^\lambda g_t(\mathbf{x})\mathrm{d}t - 1\right) + 1\right)\mathrm{d}\mathbf{x} + (1-\lambda)\int_\Omega \|T^*(\mathbf{x}) - \mathbf{x}\|^2 p_\lambda(\mathbf{x})\mathrm{d}\mathbf{x}$$

$$= \mathrm{KL}(p_\lambda \| p_0) + \int_{\Omega^2} \|\mathbf{x}_0 - \mathbf{x}_1\|^2 \mathrm{d}\pi^*(\mathbf{x}_0, \mathbf{x}_1)$$

$$= \mathcal{J}_{\mathrm{sot}}(\pi^*)$$

Thus, $\mathcal{J}_{\mathrm{sot}}(\pi^*) = \mathcal{J}^\lambda_{\mathrm{tpt}}(v_t, g_t) \geq \min_{v_t, g_t} \mathcal{J}^\lambda_{\mathrm{tpt}}(v_t, g_t)$.

(2) To show the reverse inequality $\min_\pi \mathcal{J}_{\mathrm{sot}}(\pi) \leq \min_{v_t, g_t} \mathcal{J}^\lambda_{\mathrm{tpt}}(v_t, g_t)$, we assume the contrary that $\min_\pi \mathcal{J}_{\mathrm{sot}}(\pi) > \min_{v_t, g_t} \mathcal{J}^\lambda_{\mathrm{tpt}}(v_t, g_t)$. Let (v_t^*, g_t^*) be an optimal solution to problem (5), and define

$$\tilde{p}_\lambda(\mathbf{x}) := p_0(\mathbf{x})\exp\left(\int_0^\lambda g_t^*(\mathbf{x})\mathrm{d}t\right),$$

Since the second-stage evolution p_t, for $t \in (\lambda, 1]$, is governed solely by the velocity field v_t and does not involve mass creation or destruction, both $\tilde{p}_\lambda$ and p_1 have the same total mass. Thus, the Monge map $\tilde{T}^*$ from $\tilde{p}_\lambda$ to p_1 under quadratic cost is well-defined. Then, by the Benamou–Brenier formulation [58, 59], we have

$$v_t^*\left(\mathbf{x} + \frac{t-\lambda}{1-\lambda}(\tilde{T}^*(\mathbf{x}) - \mathbf{x})\right) = \frac{\tilde{T}^*(\mathbf{x}) - \mathbf{x}}{1-\lambda},$$

and the corresponding coupling $\tilde{\pi}^* := (\mathrm{Id}, \tilde{T}^*)_{\#}\tilde{p}_\lambda$ satisfies

$$\mathcal{J}_{\mathrm{sot}}(\tilde{\pi}^*) = \mathrm{KL}(\tilde{p}_\lambda \| p_0) + \int_{\Omega^2} \|\mathbf{x}_0 - \mathbf{x}_1\|^2 \mathrm{d}\tilde{\pi}^*(\mathbf{x}_0, \mathbf{x}_1)$$

$$= \int_\Omega p_0(\mathbf{x})\left(e^{\int_0^\lambda g_t^*(\mathbf{x})\mathrm{d}t}\left(\int_0^\lambda g_t^*(\mathbf{x})\mathrm{d}t - 1\right) + 1\right)\mathrm{d}\mathbf{x} + (1-\lambda)\int_\Omega \|v_t^*(\mathbf{x})\|^2 \tilde{p}_\lambda(\mathbf{x})\mathrm{d}\mathbf{x}$$

$$= \mathcal{J}^\lambda_{\mathrm{tpt}}(v_t^*, g_t^*) = \min_{v_t, g_t} \mathcal{J}^\lambda_{\mathrm{tpt}}(v_t, g_t) < \min_\pi \mathcal{J}_{\mathrm{sot}}(\pi)$$

which leads to the contradiction.

Combining (1) and (2), we have $\mathcal{J}_{\mathrm{sot}}(\pi^*) = \mathcal{J}^\lambda_{\mathrm{tpt}}(v_t^*, g_t^*)$.

Given π^*, we construct g_t^*, v_t^* as in Eq. (A-18). According to the proof of (1), we have $\mathcal{J}^\lambda_{\mathrm{tpt}}(v_t^*, g_t^*) = \mathcal{J}_{\mathrm{sot}}(\pi^*) = \min_{v_t, g_t} \mathcal{J}^\lambda_{\mathrm{tpt}}(v_t, g_t)$. □

A.3 Proof and Empirical Evidence of Theorem 1

For the convenience of reading, here we restate Theorem 1 in the main text as Theorem A-3.

Theorem A-3. *Gvien the initial distribution p_0, denote the ending distribution of the two-period dynamics*

$$\partial_t p_t = g_t p_t, t \in [0, \lambda]; \quad \partial_t p_t = -\nabla \cdot (p_t v_t), t \in (\lambda, 1], \tag{A-19}$$

as p_1, and denote the ending distribution of the joint dynamics starting from p_0

$$\partial_t \tilde{p}_t = -\nabla \cdot (\tilde{p}_t \tilde{v}_t) + \tilde{g}_t \tilde{p}_t, \quad t \in [0, 1], \quad \tilde{p}_0 = p_0, \tag{A-20}$$

as $\tilde{p}_1$, then it holds that $\tilde{p}_1 = p_1$.

Proof. Given $\mathbf{x}_0 \sim p_0$, consider the two systems below.

System I (original two-period transport dynamics):

$$\begin{cases} \dfrac{\mathrm{d}\mathbf{x}_t}{\mathrm{d}t} = v_t(\mathbf{x}_t) \cdot \mathbb{I}_{(\lambda,1]}(t), \\ \dfrac{\mathrm{d}}{\mathrm{d}t} \log w_t(\mathbf{x}_t) = g_t(\mathbf{x}_t) \cdot \mathbb{I}_{[0,\lambda]}(t), \end{cases} \tag{A-21}$$

where w_t is the time-dependent weight function.

System II (joint dynamics defined via reparameterization (6)):

$$\begin{cases} \dfrac{\mathrm{d}\mathbf{x}_t}{\mathrm{d}t} = \tilde{v}_t(\mathbf{x}_t), \\ \dfrac{\mathrm{d}}{\mathrm{d}t} \log w_t(\mathbf{x}_t) = \tilde{g}_t(\mathbf{x}_t), \end{cases} \tag{A-22}$$

with $\tilde{w}_t$ being the time-dependent weight under joint dynamics. We first recall the definition $\tilde{v}_t(\mathbf{x}) = (1 - \lambda) \cdot v_{(1-\lambda)t+\lambda}(\mathbf{x}), \tilde{g}_t(\mathbf{x}) = \lambda \cdot g_{\lambda t}\left(\psi_{\tilde{v},t}^{-1}(\mathbf{x})\right)$. To prove Theorem 1, it suffices to show that given the same initialization $\mathbf{x}_0, w_0(\mathbf{x}_0)$, the final state of system I $(\mathbf{x}_1, w_1(\mathbf{x}_1))$ and II $(\tilde{\mathbf{x}}_1, \tilde{w}_1(\tilde{\mathbf{x}}_1))$ are identical, *i.e.*, $\tilde{\mathbf{x}}_1 = \mathbf{x}_1$ and $\tilde{w}_1(\tilde{\mathbf{x}}_1) = w_1(\mathbf{x}_1)$.

$$\begin{aligned} \tilde{\mathbf{x}}_1 &= \mathbf{x}_0 + \int_0^1 \tilde{v}_t(\mathbf{x}) \, \mathrm{d}t \\ &= \mathbf{x}_0 + \int_0^1 v_{(1-\lambda)t+\lambda}(\mathbf{x}) \cdot (1 - \lambda) \, \mathrm{d}t \\ &= \mathbf{x}_0 + \int_\lambda^1 v_s(\mathbf{x}) \, \mathrm{d}s \quad (\text{let } s = (1 - \lambda)t + \lambda) \\ &= \mathbf{x}_1. \end{aligned}$$

Meanwhile,

$$\begin{aligned} \log w_1(\mathbf{x}_1) &= \log w_\lambda(\mathbf{x}_\lambda) = \log w_\lambda(\mathbf{x}_0) \\ &= \log w_0(\mathbf{x}_0) + \int_0^\lambda g_s(\mathbf{x}_0) \, \mathrm{d}s \\ &= \log w_0(\mathbf{x}_0) + \int_0^1 \lambda \cdot g_{\lambda t}(\mathbf{x}_0) \, \mathrm{d}t \quad (\text{let } t = \frac{1}{\lambda} s) \\ &= \log w_0(\mathbf{x}_0) + \int_0^1 \lambda \cdot g_{\lambda t}(\psi_{\tilde{v},t}^{-1}(\mathbf{x})) \, \mathrm{d}t \quad (\mathbf{x} = \mathbf{x}_0 + \int_0^t \tilde{v}_s(\mathbf{x}) \mathrm{d}s) \\ &= \log w_0(\mathbf{x}_0) + \int_0^1 \tilde{g}_t(\mathbf{x}) \, \mathrm{d}t \\ &= \log \tilde{w}_1(\tilde{\mathbf{x}}_1). \end{aligned}$$

Hence, the final state and mass at $t = 1$ under both systems coincide. Applying the above analysis to all $\mathbf{x}_0 \sim p_0$ completes the proof. $\qquad \square$

Empirical evidence of Theorem 1. We provide the following example as an evidence to Theorem 1. Set $p_0 = \mathcal{N}(2, 0.5)$, $v_t(\mathbf{x}) = 2t$, $g_t(\mathbf{x}) = -\log(\mathbf{x} + 1) + t^3$, using Eq.(6), we have $\tilde{v}_t(\mathbf{x}) = (1 - \lambda)v_{(1-\lambda)t+\lambda}(\mathbf{x})$, $\tilde{g}_t(\mathbf{x}) = \lambda g_{\lambda t}(\psi_{\tilde{v},t}^{-1}(\mathbf{x})) = \lambda g_{\lambda t}(\mathbf{x} - ((1 - \lambda)t + \lambda)^2 + \lambda^2)$. By setting $\lambda = 0.4$ and using numerical solvers to solve the corresponding continuity equation, we validate our correctness of our theorem. As shown in Fig. A-5, the two dynamics ended in the same distribution.
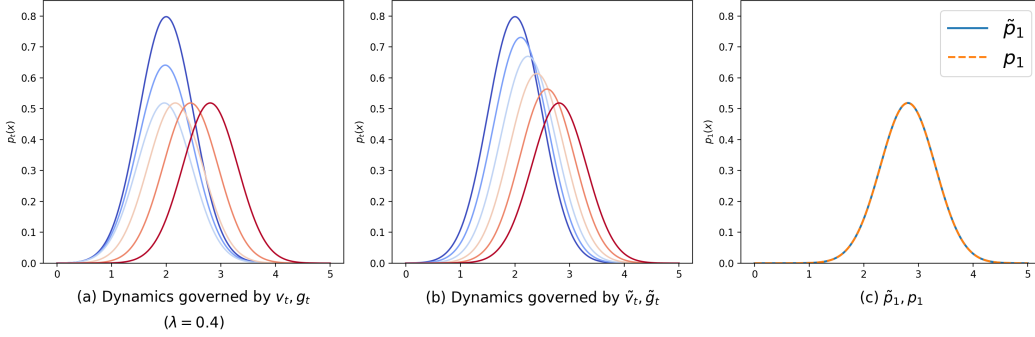
Figure A-5: Empirical evidence of Theorem 1.(a) original two-period transport dynamics. (b) joint dynamics defined via reparameterization 6. (c) the two dynamics ended in the same distribution.

A.4 Choosing $\tilde{g}_t$ According to Eq. (9) Minimizes the L^2-norm Energy Functional

We aim to prove the following statement: Given a function $w_t(\mathbf{x})$ whose logarithmic derivative satisfies $\frac{\mathrm{d}}{\mathrm{d}t} \log w_t(\mathbf{x}) = g_t(\mathbf{x})$ and the boundary condition

$$\log w_1(\mathbf{x}) - \log w_0(\mathbf{x}) = \int_0^1 g_t(\mathbf{x}) \, \mathrm{d}t,$$

then among all functions $g_t(\mathbf{x})$ satisfying this constraint, the one minimizing the energy functional

$$\mathcal{E}(g) := \int_\Omega \int_0^1 \|g_t(\mathbf{x})\|_2^2 \, \mathrm{d}t \mathrm{d}\mathbf{x}$$

is the constant function $\int_0^1 g_t(\mathbf{x})\mathrm{d}\mathbf{x} = \log w_1(\mathbf{x}) - \log w_0(\mathbf{x})$. To show this, we apply the method of Lagrange multipliers. Introduce a multiplier $\lambda(\mathbf{x})$ and consider the Lagrangian

$$\mathcal{L}(g_t) = \int_\Omega \left(\int_0^1 \left(g_t(\mathbf{x})^2 + \lambda(\mathbf{x}) \, g_t(\mathbf{x}) \right) \mathrm{d}t - \lambda(\mathbf{x}) \left(\log w_1(\mathbf{x}) - \log w_0(\mathbf{x}) \right) \right) \mathrm{d}\mathbf{x}.$$

Taking the first variation of $\mathcal{L}$ with respect to $g_t(\mathbf{x})$ yields the optimality condition

$$\frac{\delta \mathcal{L}}{\delta g_t}(\mathbf{x}) = 2g_t(\mathbf{x}) + \lambda(\mathbf{x}) = 0 \;\Rightarrow\; g_t(\mathbf{x}) = -\frac{\lambda(\mathbf{x})}{2}.$$

This shows that the optimal $g_t(\mathbf{x})$ is constant with respect to time. Plugging this into the constraint gives $g_t(\mathbf{x}) = \log w_1(\mathbf{x}) - \log w_0(\mathbf{x})$. Hence, the constant function $g_t(\mathbf{x})$ is the unique minimizer of the energy functional under the given constraint.

B Experimental Details

The model architecture has been described in Sect. 4. We next detail the strategy for selecting the hyperparameters ϵ and τ in Eq. (11), as well as provide a comprehensive description of each experiment. All experiments are performed on a single-core CPU without GPU acceleration, and all visualizations are based on projections onto the first two dimensions of the high-dimensional data.
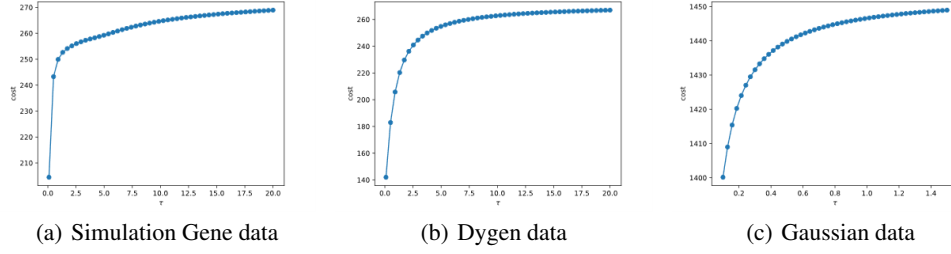
(a) Simulation Gene data   (b) Dygen data   (c) Gaussian data

Figure A-6: Fixing $\epsilon = 0.001$, we plot the transport cost as a function of τ. (a) In Simulation Gene, the curve flattens around $\tau = 5$; (b) In Dyngen, the transport cost also stabilizes near $\tau = 5$.

B.1 Determine the Entropy Regularization Parameter ϵ and Relaxation Coefficient τ

Our algorithm involves solving a static semi-relaxed optimal transport problem (11), which includes two critical hyperparameters ϵ and τ. These parameters play a pivotal role in the behavior and stability of the model. On one hand, if ϵ is too small, it may lead to numerical instability; if it is too large, it can cause incorrect cross-branch matching in unbalanced data scenarios. To select ϵ, we first set τ to a moderately large value, such as $\tau = 50$, and then perform a grid search over increasing values of ϵ starting from 0 until numerical stability is achieved. The choice of τ is even more crucial. When τ is too small, the KL divergence term between $P_{\#}^0 \pi$ and p_0 receives a weak penalty. As a result, the transport mass becomes overly concentrated around points close to p_1, leading to highly uneven marginals $\pi \mathbf{1}_m$ in the discrete setting. This causes instability in the learning of the growth function g and may result in erroneous modeling. Conversely, as $\tau \to +\infty$, Eq. (11) reduces to a balanced OT problem, which contradicts the unbalanced nature of our formulation. To determine a suitable value for τ, we fix the previously selected small ϵ and gradually increase τ while observing the variation in $\sum \pi_{ij} c_{ij}$. This curve typically exhibits an increasing-then-flattening trend. Similar to the "elbow metho" used in clustering to select the optimal number of clusters, we identify the region where the curve becomes stable and choose τ accordingly, as illustrated in Fig. A-6.

On the *simulation gene* dataset, we fix $\epsilon = 0.001$ and evaluate the model with different values of $\tau \in \{5, 10, 15, 20\}$, all of which lie within the identified stable region. The corresponding model performance metrics are summarized in Tab. A-4. We observe that the models trained with τ in this range are stable, validating the effectiveness of our hyperparameter selection strategy.

Table A-4: Fix $\epsilon = 0.001$, change different τ on simulation gene data, we present the Wasserstein-1 distance of each timepoint.

Models	t_1		t_2		t_3		t_4	
	$\mathcal{W}_1$	RME	$\mathcal{W}_1$	RME	$\mathcal{W}_1$	RME	$\mathcal{W}_1$	RME
VFGM ($\tau = 5$)	0.046	0.007	0.062	0.001	0.053	0.003	0.063	0.003
VFGM ($\tau = 10$)	0.041	0.005	0.053	0.005	0.038	0.007	0.040	0.008
VFGM ($\tau = 15$)	0.045	0.003	0.056	0.003	0.046	0.005	0.052	0.004
VFGM ($\tau = 20$)	0.043	0.007	0.057	0.004	0.045	0.007	0.058	0.011

B.2 Simulation of Gene Data

Following the setup of [25], the dynamics of the simulated gene regulatory network are governed by the following system of differential equations:

$$\frac{\mathrm{d}X_1}{\mathrm{d}t} = \frac{\alpha_1 X_1^2 + \beta}{1 + \alpha_1 X_1^2 + \gamma_2 X_2^2 + \gamma_3 X_3^2 + \beta} - \delta_1 X_1 + \eta_1 \xi_t,$$

$$\frac{\mathrm{d}X_2}{\mathrm{d}t} = \frac{\alpha_2 X_2^2 + \beta}{1 + \gamma_1 X_1^2 + \alpha_2 X_2^2 + \gamma_3 X_3^2 + \beta} - \delta_2 X_2 + \eta_2 \xi_t, \qquad \text{(A-23)}$$

$$\frac{\mathrm{d}X_3}{\mathrm{d}t} = \frac{\alpha_3 X_3^2}{1 + \alpha_3 X_3^2} - \delta_3 X_3 + \eta_3 \xi_t,$$

where $X_i(t)$ denotes the expression level of gene i at time t. Genes X_1 and X_2 mutually inhibit each other while self-activating, forming a toggle-switch regulatory motif. An external signal β independently activates both X_1 and X_2, whereas X_3 inhibits the expression of both X_1 and X_2.

The parameters α_i and γ_i determine the strengths of self-activation and inhibition, respectively. The δ_i terms denote degradation rates, and $\eta_i \xi_t$ represents additive Gaussian noise with intensity η_i. The cell division rate is positively correlated with X_2 expression and is calculated as

$$g = \frac{\alpha_2 X_2^2}{1 + X_2^2} \%.$$

At each cell division event, daughter cells inherit gene expression values (X_1, X_2, X_3) from the parent, subject to small perturbations $\eta_d \mathcal{N}(0, 1)$ per gene. Post-division, cells evolve independently according to the same stochastic dynamics.

Initial Conditions and Simulation Setup. Initial expression states are sampled from two normal distributions: $\mathcal{N}([2, 0.2, 0], 0.01)$ and $\mathcal{N}([0, 0, 2], 0.01)$. At every step, negative values are clipped to zero. Gene expression data is recorded at time points $t \in \{0, 8, 16, 24, 32\}$.

By setting $\tau = 10$ and $\epsilon = 0.001$ according to our selection scheme described in Appendix B.1 and illustrated in Fig. A-6 (a), we train the model with a warm-up stage of 200 iterations. After that, distribution fitting loss $\mathcal{L}_{\mathrm{OT}}$ is introduced for an additional 30 training epochs. Our model achieve the best performance in terms of (weighted) $\mathcal{W}_1$ and relative mass error as shown in Tab. 1.

Table A-5: Simulation parameters on gene regulatory network [25].

Parameter	Value	Description
α_1	0.5	Strength of self-activation for X_1
γ_1	0.5	Inhibition of X_2 by X_1
α_2	1	Strength of self-activation for X_2
γ_2	1	Inhibition of X_1 by X_2
α_3	1	Strength of self-activation for X_3
γ_3	10	Half-saturation constant for inhibition
δ_1	0.4	Degradation rate for X_1
δ_2	0.4	Degradation rate for X_2
δ_3	0.4	Degradation rate for X_3
η_1	0.05	Noise intensity for X_1
η_2	0.05	Noise intensity for X_2
η_3	0.05	Noise intensity for X_3
η_d	0.014	Noise for perturbation during cell division
β	1	External activation signal
$\mathrm{d}t$	1	Simulation time step
Time Points	$\{0, 8, 16, 24, 32\}$	Observation time points

B.3 Dyngen Data

Dyngen is a multi-modal simulation engine for studying dynamic cellular processes at single-cell resolution [52]. We follow the setup of [30], which simulates gene expression time-series data that

mimics cell proliferation processes, including branching and temporal progression. In the analyzed instance of the `dyngen` dataset, the samples span five discrete time points, labeled from 0 to 4, capturing the temporal evolution of the cell population.

We use PHATE [53] to reduce its dimensions to 5, the same as [30]. Starting from time point 0, cells can be divided into two branches based on the sign of the second PHATE coordinate (x_2). Quantitative analysis reveals a pronounced branch imbalance: for instance, at time point 4, 88 cells belong to one branch while 213 belong to the other, which poses a great challenge to the models that do not consider unbalancedness, resulting in cross-branch inference. Throughout this study, we assume that the temporal change in cell counts within each branch is entirely governed by a growth function, without contributions from migration or observational noise.

By setting $\tau = 5$ and $\epsilon = 0.03$ according to our selection scheme described in Appendix B.1 and illustrated in Fig. A-6 (b), we train the model with a warm-up stage of 400 iterations. After that, distribution fitting loss $\mathcal{L}_{\mathrm{OT}}$ is introduced for an additional 30 training epochs. Our model successfully avoids cross-branch reconstructions in trajectory modeling, as illustrated in Fig. A-7. This leads to generated samples that remain well-aligned with the underlying manifold. In terms of growth rate estimation, our model also accurately captures the rapid expansion observed in the branch below between time point 3 and time point 4, where the number of observed cells increases dramatically from 25 to 213, indicating the highest growth rate in the system.
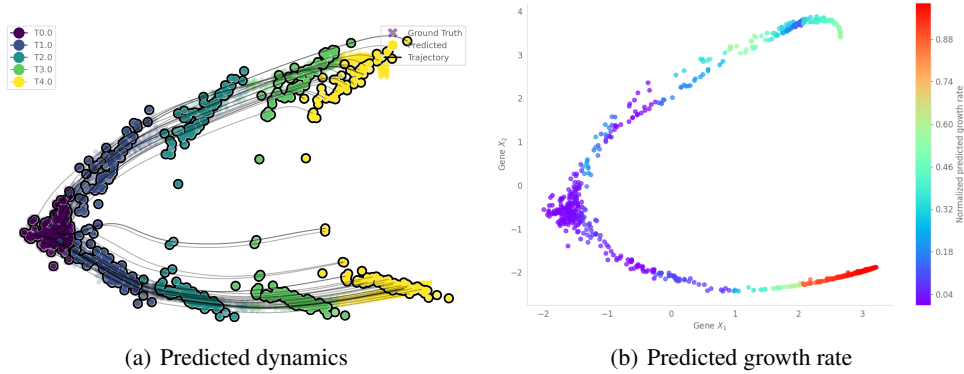

(a) Predicted dynamics   (b) Predicted growth rate

Figure A-7: Predicted dynamics and growth rates by VGFM on Dyngen data.

B.4   Gausssian 1000D Data

DeepRUOT [25] employs a high-dimensional Gaussian mixture distribution (100D) [54] to evaluate the scalability of models. In this work, we adopt an even more challenging setting by testing scalability at 1000 dimensions. Following the setup of [25], for the initial distribution, we generated 400 samples from the Gaussian located lower in the (x_1, x_2) plane, and 100 samples from the Gaussian positioned higher. For the final distribution, we generated 1,000 samples from the upper Gaussian, and 200 samples each from the two lower Gaussians, and assume cells in the upper region exhibit proliferation without transport [5]. We observe that simulation-based methods [25] encounter training instability in the 1000-dimensional setting and flow matching-based methods fail to learn a reliable velocity field due to the unbalancedness of data, as shown in Tab. 1. (Some works incorporating unbalancedness [35, 40] may as well reconstruct correct velocity field but fail to construct growth rate). In contrast, By setting $\tau = 5$ and $\epsilon = 0.03$ according to our selection scheme described in Appendix B.1 and illustrated in Fig. A-6 (c), we train the model with a warm-up stage of 500 iterations. After that, distribution fitting loss $\mathcal{L}_{\mathrm{OT}}$ is introduced for an additional 10 training epochs. Our method remains effective even in high-dimensional regimes for both velocity and growth field learning.
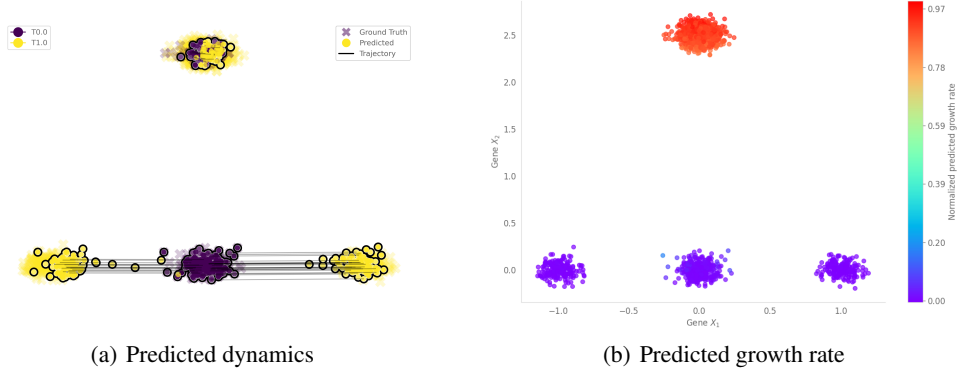
20

(a) Predicted dynamics   (b) Predicted growth rate

Figure A-8: Predicted dynamics and growth rates by VGFM on Gaussian 1000D data.

B.5 Additional Experiment: Mouse Hematopoiesis Data

We also validate our algorithm on the mouse hematopoiesis data previously analyzed in [22, 25, 60]. This dataset leverages lineage tracing to track differentiation trajectories. After applying batch correction to integrate data across multiple experiments, the cells were embedded into a two-dimensional force-directed layout (SPRING plot). The resulting visualization reveals a pronounced bifurcation, where early progenitor cells diverge into two distinct differentiation lineages.

(a) Predicted dynamics   (b) Predicted growth rate
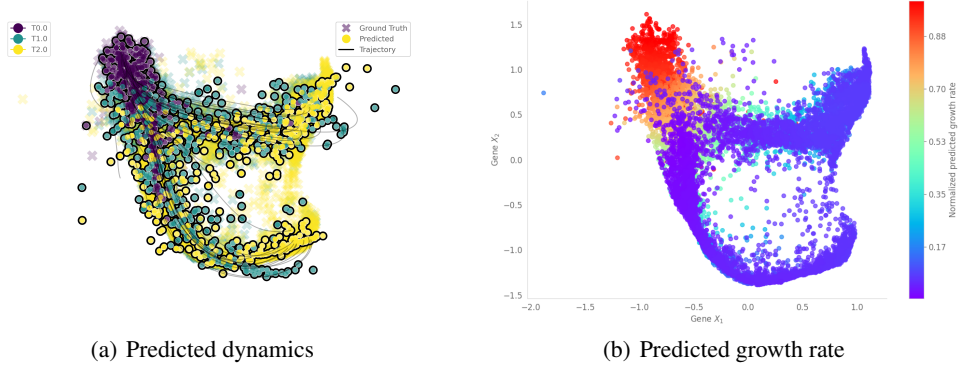
Figure A-9: Predicted dynamics and growth rates by VGFM on mouse hematopoiesis data.

Our model effectively captures the underlying branching structure in the data, and the predicted growth rates align well with those reported in [25], as well as with established biological priors and are consistent with known biological lineage patterns. Following the evaluation protocol of [25], we also compute the Wasserstein-1 distance as a quantitative metric. Under this evaluation, by setting $\tau = 20$ and $\epsilon = 0.005$ according to our selection scheme described in Appendix B.1, we train the model with a warm-up stage of 200 iterations. After that, the distribution fitting loss $\mathcal{L}_{\text{OT}}$ is introduced for an additional 50 training epochs. Our method achieves superior performance, demonstrating improved trajectory inference. In addition, we evaluate the RME (Relative Mass Error) metric introduced in this paper. The results indicate that our model significantly outperforms the other baselines in terms of mass-matching reconstruction accuracy, as shown in Tab. A-6 and Fig. A-10.

Table A-6: $\mathcal{W}_1$ and RME over all time on mouse hematopoiesis data. Part of the results were adopted from [25].

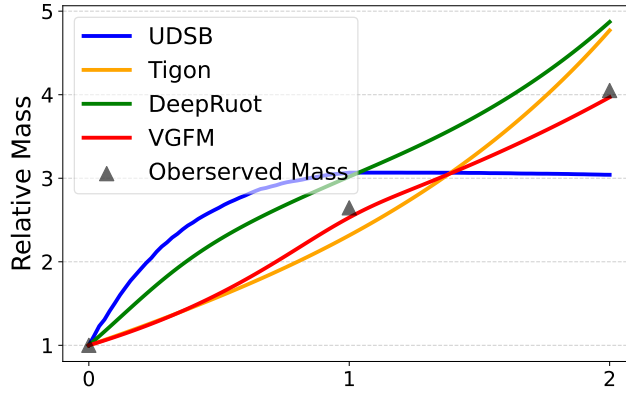| Models	t_1		t_2	
	$\mathcal{W}_1$	RME	$\mathcal{W}_1$	RME
SF^{2}M [39]	0.167	—	0.190	—
uAM[42]	0.745	—	0.777	—
UDSB [49]	0.388	0.159	0.128	0.249
TIGON [22]	0.314	0.124	0.342	0.177
DeepRUOT [25]	0.145	0.140	0.132	0.202
VGFM	**0.115**	**0.043**	**0.094**	**0.019**

Figure A-10: Comparison of predicted relative mass (UDSB, TIGON, DeepRUOT, VFGM) with observed values from mouse hematopoiesis data.

B.6   EB Data

Extensive experiments on the Embryoid Body (EB) [55] dataset with varying PCA dimensions are conducted in Sect. 4. We preprocess this dataset first by normalizing EB (5D) and leaving EB (50D) unnormalized. The proposed VFGM demonstrates strong performance in both cellular dynamics reconstruction and growth prediction, as illustrated in Fig. A-11. Specifically, we set the parameters as $\epsilon = 0.01$, $\tau = 30$, $M_1 = 800$, and $M_2 = 830$, and normalize the cost matrix to ensure numerical stability when computing the semi-relaxed optimal transport plans (Eq. (11)).

Big batch strategy for large-scale datasets. When the number of observed data points is large, computing the transport plan between two consecutive time points using Eq. (11) becomes computationally inefficient. To address this, we adopt a Big-Batch Strategy. Specifically, we partition the data at each time point into n subsets, referred to as Big Batches. For each of the n Big Batches, we precompute and store the transport plans between adjacent time points. During training, we randomly select one Big Batch and sample smaller mini-batches from it based on the precomputed transport plan for model optimization. In real-world datasets, we set $n = 5$, while in synthetic datasets above we do not apply this strategy, *i.e.*, $n = 1$, as the sample size is relatively smaller. The mini-batch size is set to 256 for all experiments, except for Dyngen, where we use a smaller batch size of 32 due to its limited number of samples.
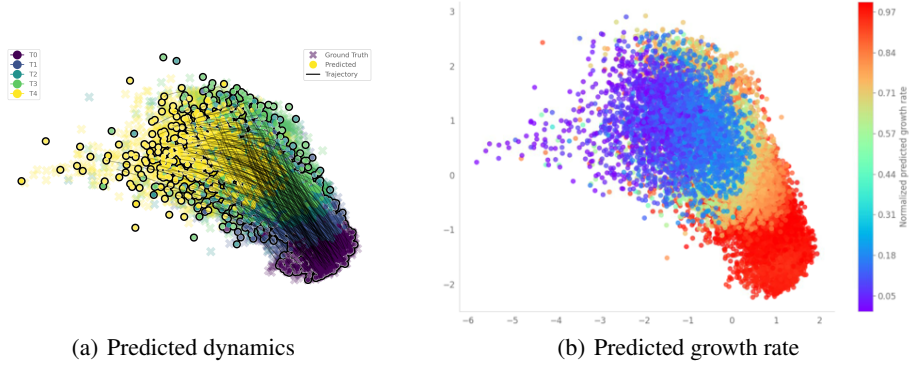
(a) Predicted dynamics

(b) Predicted growth rate

Figure A-11: Predicted dynamics and predicted growth rates by VGFM on 5D EB data with timepoint 1 held out.

We also examine whether the distribution fitting loss might lead to overfitting on the given population snapshots. In the hold-one-out experiments (Tab. 2), we relabel the timestamps of the four timepoints as 0, 1, 2, 3, and 4. Following the protocol in [36], we evaluate the model by holding out one intermediate timepoint at a time (*i.e.*, 1, 2, and 3) and report the average Wasserstein-1 distance. While hold-one-out experiments have already validated the superiority of VFGM over other methods, we further analyze the loss curves of both the distribution fitting loss and the $\mathcal{W}_1$ distance on a hold-out distribution (*e.g.*, the distribution at time 1) that is not seen during training (Fig. A-12). The results show that the $\mathcal{W}_1$ distance on the hold-out distribution decreases during the optimization of $\mathcal{L}_{\mathrm{OT}}$, indicating the absence of overfitting and demonstrating the generalization ability of the distribution fitting loss in modeling unseen distributions.
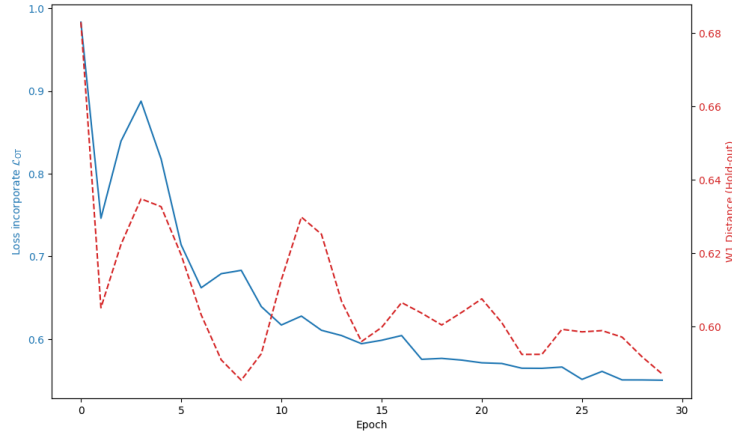

Figure A-12: Loss curves of the training loss after incorporating $\mathcal{L}_{\mathrm{OT}}$ (blue) and the $\mathcal{W}_1$ distance on a hold-out distribution at timepoint 1 (red) on 5D EB data.

B.7 CITE Data

CITE-seq (Cellular Indexing of Transcriptomes and Epitopes by Sequencing) [56] is an advanced technique that enables the simultaneous profiling of transcriptomes and surface protein expression at the single-cell level through the use of antibody-derived tags. In this study, we utilize only the gene expression matrix from the CITE-seq dataset, and preprocess the data by normalizing CITE (5D) and leaving CITE (50D) unnormalized. The experimental settings for the CITE dataset are consistent with those used in the EB data experiments, employing PCA with 5 and 50 dimensions, and hyperparameters set as $\epsilon = 0.01$, $\tau = 30$, $M_1 = 800$, and $M_2 = 830$. We relabel the timestamps of the four timepoints as 0, 1, 2, and 3. Following the protocol in [36], we evaluate the model by

holding out one intermediate timepoint at a time (*i.e.*, 1 and 2) and report the average Wasserstein-1 distance.

To assess the model's capability to capture state trajectories (Fig. A-13 (a)) and predict mass growth (Fig. A-13 (b)), the distribution at time point 1 is held out. Additionally, the distribution at time point 2 is held out to evaluate the performance of the $\mathcal{L}_{OT}$ and $\mathcal{W}_1$ distance (hold-out) curves (Fig. A-14). The strong performance observed in the visualizations substantiates the potential of the proposed VGFM framework.
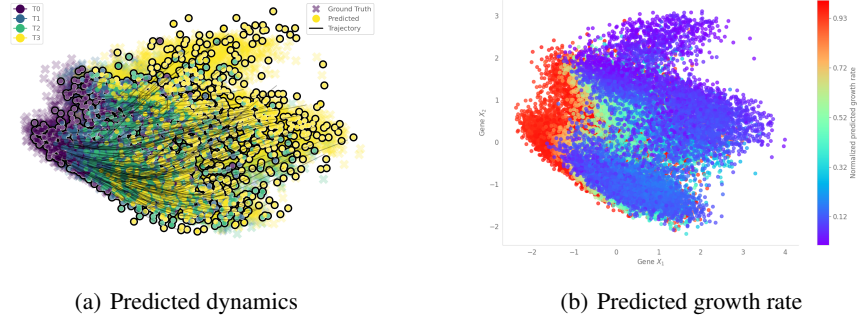

(a) Predicted dynamics   (b) Predicted growth rate

Figure A-13: Predicted dynamics and predicted growth rates by VGFM on 5D CITE Data with timepoint 1 held out.

(a) 5D CITE data with hold out timepoint 2   (b) 50D CITE data with hold out timepoint 2
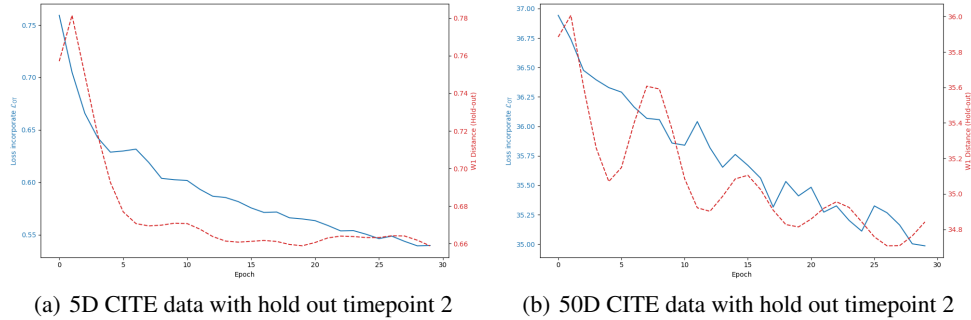
Figure A-14: Loss curves of the training loss after incorporating $\mathcal{L}_{OT}$ (blue) and the $\mathcal{W}_1$ distance on a hold-out distribution at timepoint 2 (red) on (a) 5D CITE data and (b) 50D CITE data.

C   Broader Impacts

Our method provides a scalable and efficient framework for modeling cellular dynamics, enabling trajectory reconstruction and growth rate inference in high-dimensional single-cell datasets. In biomedical and clinical settings, such capabilities can facilitate a deeper understanding of developmental processes, disease progression, and response to treatment at a single-cell resolution. For example, modeling differentiation trajectories and proliferation patterns of stem or immune cells could inform therapeutic strategies in cancer, regenerative medicine, and immunotherapy.

However, the proposed method is inherently data-driven and relies on statistical patterns learned from observational data. As such, it may produce biologically implausible trajectories or growth behaviors that conflict with known biological priors, especially when the training data is noisy, biased, or incomplete. This could potentially lead to misleading interpretations or incorrect clinical hypotheses if not carefully validated by domain experts. Therefore, we emphasize that any downstream medical conclusions drawn from the model's output should be interpreted with caution and in conjunction with biological prior knowledge and experimental validation.